

# Refinement and Validation of MRI-Based Models for Joint Contact Mechanics

By

ALEXANDER JEFFREY WALLER

Submitted to the Department of Mechanical Engineering and the Graduate School of  
Engineering of the University of Kansas  
In partial fulfillment of the requirements for the degree of

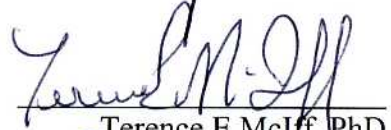
Master of Science in Mechanical Engineering

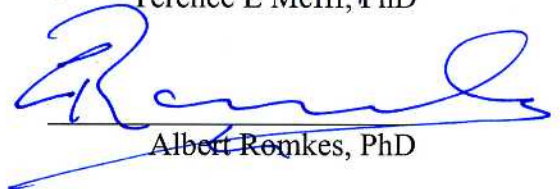
Chairperson:

  
Kenneth J Fischer, PhD

Committee Members:

  
Lorin P Maletsky, PhD

  
Terence E McIff, PhD

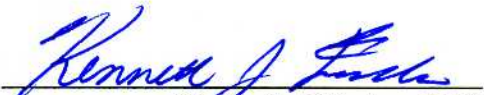
  
Albert Romkes, PhD

Date Defended: 29 June 2007

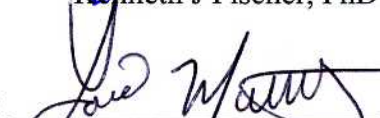
The Thesis Committee for ALEXANDER JEFFREY WALLER certifies that this is the approved version of the following thesis:

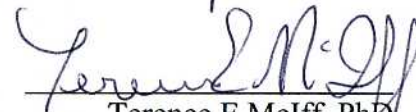
## Refinement and Validation of MRI-Based Models for Joint Contact Mechanics

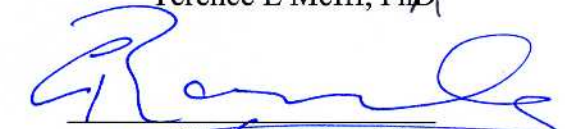
Chairperson:

  
Kenneth J Fischer, PhD

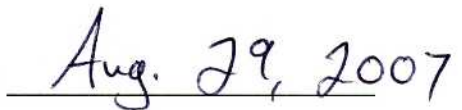
Committee Members:

  
Lorin P Maletsky, PhD

  
Terence E McIff, PhD

  
Albert Romkes, PhD

Date Approved:



## **Abstract**

The purpose of this study was to determine the validity of an MRI-based modeling technique for use in joint contact mechanics. First, the accuracy and repeatability of two experimental measures, Fuji-scale film and a piezoelectronic sensor, were tested. It was found that the piezoresistive sensor was the more accurate technique for measuring joint contact loads. Then, segmented and projected cartilage modeling techniques were compared. It was found that the two techniques had highly different contact mechanics. Finally, the MRI-based modeling technique was tested using 5 cadaveric specimens. It was found the MRI-based models and the direct measurement from MR image sets showed similar results for contact area. The Tekscan and MRI-based model technique showed similar measures of contact force, and the Pressurex and MRI-based technique showed similar measures of peak pressure. It is therefore believed that the MRI-based modeling technique is a feasible method of analyzing joint contact mechanics.

## **Acknowledgement**

The last two years have been challenging but rewarding, at times infuriatingly bromidic, and at others wildly tempestuous. This work would not have been possible without the help and support of a small army of people.

First and foremost let me express my gratitude to Dr. Kenneth J. Fischer, my graduate advisor. He took a major risk accepting me as his research assistant, and at several times I am sure he seriously contested the wisdom of that decision. However, with his faith and support, I achieved more than I thought possible for myself, and I know that none of this would have come about without his creative, genuine spirit.

I'd also like to acknowledge my graduate committee, Dr. Terry McIff, Dr. Lorin Maletsky, and Dr. Albert Romkes. I owe my thanks to Dr. Dougherty, and all the faculty of the Mechanical Engineering department, for their guidance and wisdom, and especially for the education I gained while there.

I'd like to acknowledge Hoglund Brain Imaging Center for use of their MRI scanners, and the Orthopedic Research Center at the University of Kansas Medical Center for use of their facilities and also for their assistance.

I'd especially like to acknowledge my parents. Whether it was nurture, or nature, you did a great job raising me and I will forever be in your debt. From a young age, you instilled in me an unquenchable thirst for knowledge, a vibrant curiosity, and a love of science. There are not words to describe how much I love and appreciate you both.

And finally, I should acknowledge the love of my life, Lindsay. Knowing that the sooner I got my work done, the sooner I could spend time with you was a great motivator, and will continue to be so for many years to come.

## Table of Contents

Abstract	i.
Acknowledgements	ii.
Table of Contents	iv.
Table of Figures	vi.
1. Background	1
1.1 Motivation	1
1.2 Research Goals	2
1.3 Summary of Project	3
1.4 Anatomy	6
1.4.1 Forearm Bones	6
1.4.2 Bones of the Wrist and Radiocarpal Joint	7
1.4.3 Tendons of Interest	8
1.4.4 Clinical Issues	9
1.5 Joint Modeling	11
1.5.1 Finite Element Method	12
1.5.2 Rigid Body Spring Modeling	15
1.5.3 Multi-Body Contact Modeling	18
1.5.4 Development of Accurate Models from Images	21
1.6 Validation Methods	22
1.6.1 Experiments Using Pressure Sensor in the Radiocarpal Joint	23
1.6.2 Validity of Using Pressurex Film or Tekscan Sensor	25
1.6.3 Projected Cartilage Modeling	27
1.7 References	30
2. Accuracy and Repeatability of Piezoresistive Sensor and Pressure Sensitive Film in the Radiocarpal Joint	34
2.1 Introduction	35
2.2 Materials and Methods	36
2.2.1 Idealized Tests	36
2.2.2 Tekscan Data Collection	39
2.2.3 Pressurex Data Collection	41
2.2.4 <i>In Situ</i> Testing	43
2.3 Results	45
2.3.1 Tekscan	45
2.3.2 Pressurex	45
2.3.3 <i>In Situ</i> Testing	46
2.4 Discussion	47
2.5 References	49
3. Segmented Cartilage Models vs. Cartilage Models Projected from Bones	51
3.1 Introduction	53

3.2	Materials and Methods	54
3.2.1	Wrist Preparation	54
3.2.2	Tekscan Tests	56
3.2.3	MRI Data Acquisition	58
3.2.4	Computer Modeling	59
3.3	Results	61
3.4	Discussion	65
3.5	References	67
4.	Validation of MRI-Based Modeling for Joint Contact Mechanics	71
4.1	Introduction	72
4.2	Methods	76
4.2.1	Specimen Preparation	76
4.2.2	Experimental Setup	78
4.2.3	Experimental Validation	80
4.2.3.1	Pressurex Film	80
4.2.3.2	Tekscan Sensor	83
4.2.4	Specimen Imaging and Modeling	86
4.2.5	Execution of Modeling Simulation	89
4.2.6	Direct Contact Measurement from MR Images	90
4.2.7	Statistical Analysis	91
4.3	Results	92
4.3.1	Kinematics	92
4.3.2	Summary of Experimental and Modeling Data	95
4.3.3	Direct Contact Area Measurement	97
4.3.4	Regression Analysis	99
4.4	Discussion	100
4.5	References	104
5.	Summary	108
5.1	Accuracy and Repeatability of Tekscan Sensor and Pressurex Film	108
5.2	Segmented Cartilage Models vs. Cartilage Models Projected From Bones	110
5.3	Validation of MRI-Based Joint Model	111
5.4	Implications for Future Work	112

## Table of Figures

<b>Figure 1.1</b> Pronation (A) and supination (B) of the forearm.	7
<b>Figure 1.2</b> Bones of the Wrist.	8
<b>Figure 2.1.</b> Experimental setup used in this study.	38
<b>Figure 2.2.</b> Typical regression equation, curve, and coefficients developed from Tekscan output data.	40
<b>Figure 2.3.</b> Raw Tekscan image from cylindrical object tests. (a) Smaller radius object and (b) Larger radius object.	41
<b>Figure 2.4.</b> Typical regression curve developed from Pressurex data.	42
<b>Figure 2.5.</b> Experimental setup for <i>in situ</i> test of Tekscan sensor.	44
<b>Figure 2.6.</b> Sample (250N) result from Tekscan <i>in situ</i> test.	47
<b>Figure 3.1.</b> Attachment of forearm to pulley plate assembly	56
<b>Figure 3.2.</b> Sample Data from Tekscan Sensor ( <i>in situ</i> ). S indicates radioscaphoid contact; L indicates radiolunate contact.	58
<b>Figure 3.3.</b> Three-Dimensional Plot of Radius Contours in PEd	60
<b>Figure 3.4.</b> Manually generated bone models for specimen 2. (a) Segmented cartilage (b) Projected cartilage	62
<b>Figure 3.5</b> Projected model volume as a percent of segmented model volume.	63
<b>Figure 3.6.</b> Sample pressure distributions for specimen 1. Shown here are is the articular surface of the radius (a) segmented cartilage (b) projected cartilage.	64
<b>Figure 4.1</b> Isolation and fixation of radius and ulna to PVC plate. Isolated and sutured tendons also shown.	77
<b>Figure 4.2</b> Partial experimental Setup. Shown here are the five water jugs used as weights to simulate light grasp through the tendons of the wrist.	79
<b>Figure 4.3</b> Experimental Setup. Shown here is the pulley assembly used to direct the loads from the water jugs through the three flexor and two extensor tendons. Extensor tendon lines ran under a low pulley before going over the high pulleys to the left.	79

<b>Figure 4.4</b> Cross Section of Pressurex Film (Sensor Products Inc., East Hanover, NJ)	80
<b>Figure 4.5</b> Sample calibration curve (Specimen 3) showing cubic regression equation and correlation coefficient.	82
<b>Figure 4.6</b> Wrist Sensor, Model #4201.	84
<b>Figure 4.7</b> Sample calibration curve (Specimen 2) for Tekscan sensor, showing quadratic regression equation and correlation coefficient.	85
<b>Figure 4.8</b> MR Image (left) and isolated radius bone (right) for use in kinematic registration.	87
<b>Figure 4.9</b> Radius, lunate, and scaphoid bones, the contact area is visible (a), and then isolated (b) for segmentation.	91
<b>Figure 4.10</b> Magnitude of translation of each specimen.	94
<b>Figure 4.11</b> Magnitude of rotation in degrees.	94
<b>Figure 4.12</b> Total Force measured by film, Tekscan sensor and MRI-based model. Theoretically, value should be between 85-100 N.	96
<b>Figure 4.13</b> Comparison of experimental measures, MRI-based method and direct contact area measurements for all five specimens. Radioscaphoid joint (a) and radiolunate joint (b) shown here.	98
<b>Figure 4.14</b> Plot of contact area measurement from direct-measurement method versus contact area reported from MRI-based model.	100

## Chapter 1 – Background

### 1.1 Motivation

Arthritis remains a major chronic health problem, and is a leading cause of joint swelling, pain, stiffness, and loss of quality of life. Osteoarthritis (OA), the most common form of arthritis, is characterized by joint pain and dysfunction caused by a progressive loss of articular cartilage. This loss of cartilage is due to unknown mechanisms associated with age, excessive joint loading and/or joint injury. OA has been characterized by a decrease in contact pressure in early stages, and an increase in contact pressure in late stages. Though considerable research has been dedicated to understanding the exact nature of OA, there are still many questions. Magnetic Resonance Imaging (MRI) based modeling represents a new technique to understand *in vivo* contact mechanics and ultimately help understand the causes and mechanism of cartilage degeneration. MRI-based modeling could also be applied to evaluation of surgical procedures, assessment of orthotic efficacy, and evaluation of ergonomics of tools and sports equipment. The MRI-based modeling technique exists, and initial validation is under way, but further validation must be completed before the technique can be applied to human subjects.

Validation of the MRI-based modeling technique is necessary to ensure the accuracy of future *in vivo* contact mechanics study. Validation experiments using human cadaver specimens enable collection of experimental data for direct comparison with the modeling technique.

If validated, the MRI-based modeling technique can easily be generalized for the study of other joints (beyond the radiocarpal joint reported in this work) which are complex and difficult to model.

## **1.2 Research Goals**

The primary aim of this research is the detection and prevention of arthritis in the human joints. A magnetic resonance, MRI-based modeling technique was developed to understand the causes of cartilage degeneration. This technique has been implemented, but needs to be validated before extensive human subjects study can be performed. The objective of this work is to continue and complete validation data for MRI-based joint contact modeling applied to analyze *in vivo* joint contact mechanics in the radiocarpal joint. The validation is accomplished by comparing results from a cadaveric simulated grasp experiment with the results of specimen-specific MRI-based joint contact models. This validation research has the following specific objectives:

1. Conduct experiments to test the accuracy and repeatability of the Tekscan pressure sensor and Pressurex Super-Low Film, as these are experimental benchmarks against which the joint contact model will be compared.
2. Conduct experiments on three specimens to examine the validity of direct cartilage segmentation from MRI, as opposed to segmentation of bone models with lofted cartilage applied.

3. Test 5 specimens using Pressurex film and the Tekscan sensor to measure *in vitro* radiocarpal joint contact mechanics.
4. Create specimen-specific three-dimensional models of the radiocarpal joint from MR image sets of the 5 test specimens.
5. Compare the experimental results to the MRI-based modeling results, and add these data to the three specimens already tested.

### **1.3 Summary of Projects**

The purpose of this work was to validate MRI-based modeling for joint contact mechanics. To do this, three different studies were conducted.

The first study determines the accuracy and repeatability of Pressurex Super-Low film, a static Fuji-scale film, and the Tekscan I-Scan system with sensor 4201, a piezoelectric dynamic pressure sensor. Six sets of idealized tests have been conducted using two cylindrical objects with known, different radii. The sensor or film was placed between the cylindrical object being tested and a flat plate, and then each cylindrical object was pressed against the flat plate using a servohydraulic testing machine. Using a 10-point calibration process, it was possible to determine the measured load, then compare it to the actual applied load. It was found that the Tekscan dynamic sensor was the more accurate for load measurement than Pressurex film, and is generally more robust for use in the joints.

The second experiment tested the differences between cartilage models projected from the bone surface and cartilage models segmented directly from MRI data. Three

cadaveric forearm specimens were dissected, and imaged in a 3T MRI scanner in a relaxed and in a loaded state. Applying loads to three finger flexor tendons created the loaded state. The cadaveric specimen was also tested using the Tekscan sensor, by inserting the sensor into the radiocarpal joint then applying the loads through the finger flexors. 3D models were created of the bones, and of the bones with cartilage. The bone-only models were given a 1 mm, normal projection from their surface to simulate cartilage. Both sets of models were analyzed for pressure, force and contact area measurements using the Joint\_Model program. Model data was compared to the experimental Tekscan data.

The two cartilage models had similar geometries, however the projected cartilage models had significant overestimation of contact pressure when compared to the segmented cartilage models (and the Tekscan results). The overestimation was not consistent from specimen to specimen, making it difficult to draw a conclusion about the source of errors from projected cartilage modeling.

The purpose of the third experiment was to determine the validity of MRI-based modeling for radiocarpal contact mechanics. Five cadaveric forearms were dissected so that loads could be applied to three finger flexors and two wrist extensors. The wrist was also opened so that a Tekscan sensor or Pressurex film could be inserted. The wrists were imaged in a 9.4T MRI scanner in the loaded and unloaded states. Then 3D models of the radius, scaphoid, and lunate bones with cartilage were created. The wrist models were then analyzed for contact area, contact force, and peak pressure in the radioscapoid and radiolunate joints. These data were compared to the

experimental Tekscan and Pressurex data. Contact area between bones was also directly measured from the loaded MR image sets. It was found that the MRI-based model had a significant agreement in contact area with the direct contact area measurement. The Tekscan and MRI-based model technique showed similar measures of contact force, and the Pressurex and MRI-based technique showed similar measures of peak pressure. It is therefore believed that the MRI-based modeling technique is a feasible method of analyzing joint contact mechanics.

## **1.4 Anatomy**

The human wrist is a complex, multi-bone joint. Because of the complex geometry, further research is needed to derive biomechanical measurements like joint contact areas, bone contact forces and peak contact stresses during functional activities. In order to understand this research, a brief description of forearm anatomy is given below.

### **1.4.1 Forearm Bones**

The forearm is the distal portion of the upper extremity from the elbow to the distal wrist. The forearm consists of two bones, the radius and ulna, and numerous muscles and ligaments. The radius and ulna bones contact each other at their proximal and distal ends. The annular ligament, interosseous membrane, and radioulnar ligaments stabilize the radius and ulna. They also allow the radius to rotate around the ulna during pronation (palm down) and supination (palm up) of the wrist (Fig. 1.1).

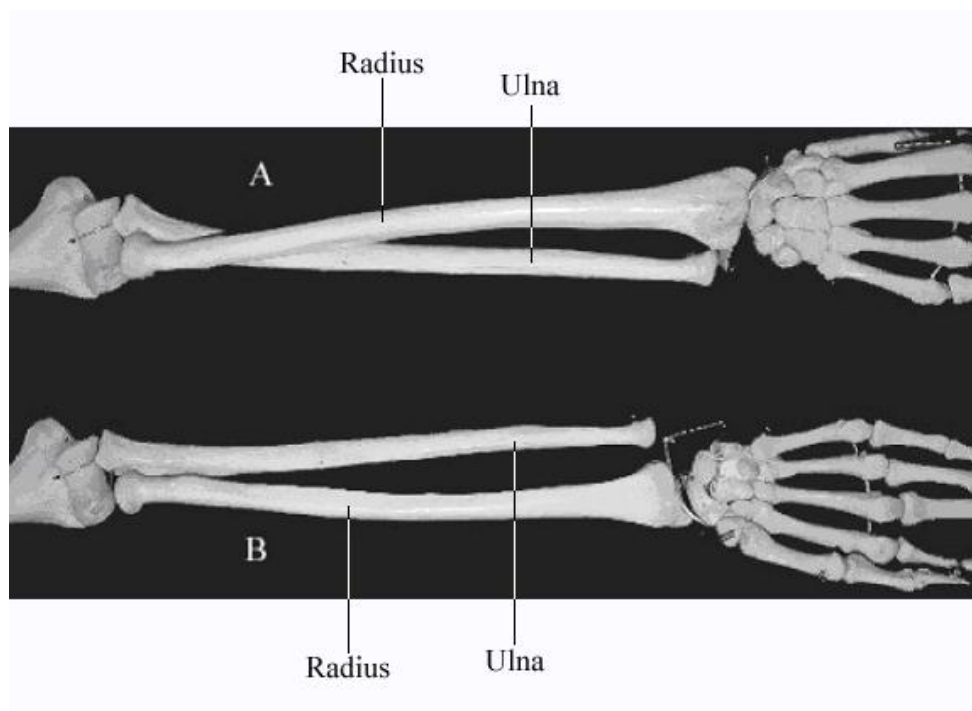


**Figure 1.1** Pronation (A) and supination (B) of the forearm.

#### **1.4.2 Bones of the Wrist and the Radiocarpal Joint**

The wrist (carpus) is a complex assembly of bones and ligaments that connects the palm (metacarpals) to the radius and ulna. The wrist consists of eight bones that create an articulation with the proximal end of the metacarpals and the distal ends of the radius and ulna. They are organized in two rows. The proximal row consists of (lateral to medial) the scaphoid, lunate, pisiform, and triquetrum. The distal row consists of the trapezoid, trapezium, capitate, and hamate. The scaphoid and lunate, and their articulation with the radius, are the subject of this study (Fig. 1.2)



**Figure 1.2** Bones of the Wrist. (From Public Domain)

The distal radius contains two concave fossa, one each for articulation with the scaphoid and lunate bones. During axial loading of the wrist, the lunate and scaphoid bones rest in these fossa, press against the radius, and each other. The radius bone carries about 80% of axial load in the wrist.<sup>14, 23</sup> It is the radiocarpal joints that will be examined in this work.

### **1.4.3 Tendons of Interest**

Muscles often attach to bones through long tendons. The wrist and hand contain a number of muscle – tendon units which create many of the motions of which the forearm and hand are capable. Three digital flexor muscles used to simulate grasp: the flexor digitorum profundus (FDP), the flexor digitorum superficialis (FDS), and the

flexor pollicis longus (FPL), which together act to flex the fingers and thumb, are of specific interest here. Two wrist extensors, the extensor carpi ulnaris (ECU) and extensor carpi radialis (longus and brevis) (ECR), are also important physiologically and in the experiment to prevent wrist flexion during grasp. When the above flexor muscles activate, pulling on their tendons, the fingers flex and the hand grasps. The two extensor muscles mentioned above normally activate during this activity, serving to keep the wrist in a neutral or slightly extended position.

#### **1.4.4 Clinical Issues**

Arthritis represents one of the most widespread chronic health problems in the human population. More than 20% of adults in the United States report arthritic conditions (<http://www.cdc.gov/arthritis/>, Accessed: 2007, 24 May). Arthritis greatly affects the aging population, as shown by the fact that 25% of those over 55 years of age report some form of arthritis.<sup>21</sup> Symptoms of arthritis include swelling, pain, and stiffness in the joints.

Osteoarthritis (OA), the most prevalent form of arthritis, is characterized by cartilage degeneration, joint pain, and joint dysfunction. In severe cases there may also be muscle degeneration and joint contractures. The loss of cartilage is believed to be caused by an unknown combination of age, excessive joint loading, and/or previous joint injury.<sup>6</sup> Osteoarthritis comes in two types: primary OA and secondary OA. Primary OA refers to the condition in which joint degeneration has an insidious

onset. Secondary OA occurs do to injury or inflammatory, metabolic, developmental, or neurological disorders.

Because sudden onset due to injury is a possible cause of OA, fractures that occur in the wrist are of interest. Fracture of the wrist can occur in several of the bones of the wrist. The most common type of wrist fracture occurs in the distal radius (Colles fracture).<sup>16</sup> The second most common is a scaphoid fracture.

Colles fracture is prevalent among adults, particularly middle-aged and elderly women who exhibit osteoporosis. Colles fracture has a high rate of malunion. Improper healing can result in shortening or angulation of the distal radius, leading to OA. Malunion could also damage the median nerve, leading to carpal tunnel syndrome.

Scaphoid fracture is another relatively common wrist fracture that often does not show obvious bone break when imaged. A scaphoid fracture can occur with little or no deformity or swelling. Scaphoid fracture accounts for about 70% of carpal bone fractures and is most common in men ages 15-30.<sup>22</sup> Scaphoid fracture is a common injury in sports and motor vehicle accidents, and is usually caused by sudden contact between the wrist and a solid, immobile object. The angle at which the wrist strikes the ground determines the fracture. If the angle is 90° or greater the scaphoid bone will likely fracture but if the wrist angle is less than 90° the distal radius more commonly fractures.<sup>22</sup>

Most scaphoid fractures occur in the proximal or middle section of the bone, hampering the blood supply to the proximal scaphoid. In extreme cases, this decrease

or loss of blood supply can lead to non-union or necrosis of the proximal fracture fragment.<sup>22</sup>

Another injury that often leads to OA of the wrist is disruption of the scapho-lunate ligament. This injury often leads to scapholunate advanced collapse (SLAC), a condition in the wrist. A common treatment method is proximal row carpectomy.<sup>8</sup> This procedure involves removal of the proximal wrist bones – scaphoid, lunate, and triquetrum, creating a new articulation between the radius and capitate bones. This new articulation is characterized by joint motion similar to pre-surgical conditions, although the joint shows a marked reduction in overall strength.

### **1.5. Joint Modeling**

Modeling is an investigative technique that uses mathematical, computer, or physical depictions of a system to conduct research on that system. A model is very useful in the exploration of biomechanical parameters affecting the human body. To understand the radiocarpal model used here, it is beneficial to have a knowledge of the methods commonly used in biomechanical engineering. The two main methods of model simulation are finite element method (FEM)<sup>2, 7, 18, 26</sup> and rigid-body spring modeling (RBSM).<sup>11, 14, 15, 19, 23</sup> The RBSM has become quite popular recently, due to its simplicity and computational efficiency in contact analysis.

Recently, a third method has been developed. This method uses a surface-based contact modeling approach which provides for generally more accurate interface and more flexible contact rules, while maintaining computational efficiency.<sup>17</sup>

### **1.5.1 Finite Element Method**

Based on a Galerkin method, the Finite Element Method (FEM) is a numerical approximation technique used to find the approximations of equivalent integral formulations of governing ordinary and/or partial differential equations. By dividing the domain into discrete pieces, and seeking polynomial approximations (linear, quadratic, cubic, etc.) on these elements, numerical approximations can be obtained. Due to the increasing power of computers, more accurate and complex analyses can be performed. Some of the advantages of FEM include accuracy of the results, convergence of approximations, and ability to determine stresses and strains inside a tissue.

However, the solution process often involves intense computation due to the many equations being solved. Often this is further complicated by the non-linearity associated with surface contact and/or material properties. Furthermore, when the material being analyzed is considered homogeneous and only surface contact is being considered, it is often unnecessary to compute the stress and strain within the tissue, as it dramatically increases computation time. Building highly accurate finite element meshes can also be time consuming even with semi-automated meshing. Automatic meshing generally yields an inferior mesh in some locations.

Anderson et al. developed a contact coupled finite element model to study the radiocarpal joint.<sup>2</sup> The 2D model of the radius, scaphoid, lunate, and cartilage surface were created using anatomical drawing and then dividing them into six elements. The

ligaments were modeled as non-linear springs that could bear only tensile loads. The modeling did not make any assumptions about load transfer across the joint. Contact was modeled using slideline elements that allow finite deformations and sliding between bodies, resisted by Coulomb friction. A frictional coefficient of 0.01 was assigned for all articular surfaces. Axial strain was plotted and it was shown that strains in the articular cartilage were about 20 to 25%. It was also demonstrated that the sliding between bones is small and did not demand a generalized contact method in that 2D model. Their model was consistent with previous experimental and computational models of the wrist.

Ulrich et al. used the 2D FEM for load transfer analysis through the trabecular network of the distal radius using high-resolution CT images.<sup>26</sup> This mesh attempted to predict fracture risk based on loading scheme. Tissue strain energy density distribution was used to characterize load transfer through the trabecular network. The wrist of a human subject was scanned using low-dose peripheral quantitative computed tomography (pQCT). This scan allowed a slice thickness of 0.165 mm. The FEM model was generated using a voxel conversion technique, and layers of cartilage of thickness 3 mm were added artificially. Four different loading regimes were applied to the carpal bones while the proximal end of the radius was fully constrained. Two FE problems were solved, each containing one of the carpal bones loaded with a unit force and the other unloaded. Post processing involved superimposing and scaling of displacement fields and calculating strain energy density and Von Mises stress. It was demonstrated that the distribution of tissue

loading *in vivo* could be estimated. The radius was found to have high strain energy values in the distal region for all loading cases which suggest that common regions of fracture are likely due to high tissue strain energy density values in the trabecular network.

Ledoux et al. used the 2D finite element method to analyze the wrist.<sup>18</sup> This study attempted to yield insight into the onset of arthritis of the wrist. X-rays of the anterior-posterior (AP) view of the wrist were used to generate bone geometry. Trapezium and trapezoid bones were modeled as a single body. The articular cartilage was modeled by non-linear, compression-only elements that constituted an interface between the bones, not as a unique structure itself. A simulated load of 100 N was applied through the metacarpals. This model predicted peak pressures at the surfaces of the lunate-capitate and scaphoid-capitate articulations and that the amount of load carried through the radiolunate fossa increased dramatically during scaphoid fracture. It was also found that scaphoid fractures caused significant increases (up to 179%) in these contact pressures.

Carrigan et al. employed the 3D FEM to analyze the wrist (radius, ulna, and all 8 carpal bones) for carpal load transmission in static neutral position.<sup>7</sup> The 3D model included bone, cartilage, and ligamentous tissues, and was based on an *in vivo* CT scan of the wrist bones in relaxed posture (converted into solid bone meshes using an ANSYS algorithm). Cartilage layers were projected from bone model surfaces, and modeled using 15-node triangular prism elements. All the solid elements were specified to have linear elastic material properties. Bone elements were given a

modulus of 10 GPa and a Poisson's ratio of 0.3. Cartilage elements were specified to have a modulus of 10 MPa and a Poisson's ratio of 0.45. A series of parametric sensitivity cases were analyzed to determine the impact of various factors like changes in cartilage modulus on contact pressures and cartilage stresses. For each of these cases, an axial load of 15 N was applied to the capitate. Results showed higher stresses at bone-cartilage interface than at the radioscaphoid cartilage surface. It was also shown that cartilage material modulus and unconstrained carpal motion can have a dramatic effect on articular contact area and pressure. The cartilage modulus showed the greatest effect, and by changing the modulus from 10 MPa to 5 MPa, a 23% reduction in contact pressure was found.

### **1.5.2 Rigid Body Spring Modeling**

The rigid body theory is a fundamental and well-established theory of physics. Rigid Body Spring Models (RBSM) are based on the assumption that force applied to the bodies produces negligible deformation. In applying this method to skeletal structures, it is presumed that the deformation of bone can be neglected when compared to the deformation of the cartilage layers at the contact surfaces. The cartilage is modeled as a set of compressive springs on the surface of the bone which is considered rigid. Ligaments are modeled as tensile springs that hold the bones together. This method provides a computationally efficient means of determining joint forces and ligament tension without the need for a more complex FE analysis.

Garcia-Elias et al. developed a 2D model of the transverse carpal arch using a RBSM.<sup>11</sup> The contours of the joints were generated from the MR images.

Compressive springs were distributed over the surface of the modeled cartilage. The ligaments of the carpal arch were modeled using tensile elastic springs. This model was then used (under simulated dorsopalmar compression) to calculate the relative motion between the carpal bones, the distribution of compressive forces in the intercarpal joint, and the tensions in the ligaments. Results showed that the palmar hamate-capitate ligament plays a significant role in stability of the carpal arch.

Horii et al., created a 2D RBSM of the wrist to evaluate the force and pressure transmission between the carpal bones.<sup>14</sup> In this model, carpal bones were modeled as rigid bodies, and connected to each other with elastic springs. X-rays were used to obtain bone geometry. Reaction forces between carpal bones were modeled using a system of linear elastic springs; cartilage was modeled as linearly compressive springs and ligaments as tensile linear springs. The spring constants were determined based on material and structural properties of ligaments and cartilage taken from literature. Axial loads were applied along the metacarpals to simulate a grasp of 10 N with the wrist in neutral position. It was found that the force transmission ratio was 55% through the radioscaphoid joint and 35% through the radiolunate joint. The remaining load was observed in the triangular fibrocartilage. The scaphoid was found to have the largest percentage of load amongst the intercarpal bones.

In a nearly identical study, Schuind et al., created a 2D RBSM of the wrist.<sup>23</sup> Schuind found similar percentages of force transmission in the three contacts

(radioscaphoid 50%, radiolunate 35%, and TFCC 15%). It was also found that the peak pressure occurred at the proximal pole of the scaphoid. Results showed no significance to age on wrist force distribution and that wrist morphology had little influence on the magnitude and pattern of load distribution.

Iwasaki et al. used a 2D RBSM of the wrist to study Kienbock's disease.<sup>15</sup> This study computed the changes in force and pressure across the wrist during the different stages of Kienbock's disease. The model was developed according to the method of Schuind et al. and Garcias-Elias et al. Twenty-four cases classified as Lichtman's stage II, IIIA, and IIIB were analyzed using the RBSM technique. Ligament tension and peak pressure were examined. Results showed that the scaphoid rotation directly affects the wrist joint contact pressure distribution pattern, and may therefore be largely responsible for Kienbock's disease. It was also shown that progression from Lichtman's stage II to IIIB showed a general increase in force transmission through the radiolunate contact, and a decrease in force transmission through the radioscaphoid contact.

Manal et al. designed a sliding rigid body spring model to study joint reaction forces in maligned juvenile wrists presenting idiopathic arthritis (JIA).<sup>19</sup> In juvenile idiopathic arthritis (due to malignment of the carpal bones), the bones are subjected to off-center loading. Large displacements cause the standard RBSM to fail because cartilage springs, intended to experience compression, report tension. In the sliding RBSM, the distal end of each compression spring is free to slide along the surface of the opposing bone contour until equilibrium is reached. AP radiographs of the wrist

from four subjects (three presenting JIA, one age-matched normal wrist) were used for modeling. The carpal bones were treated as a single body. Cartilage was modeled as linear elastic compression springs. Metacarpals were loaded axially to simulate grasp required to hold a 1 kg load. A total force of 142 N was applied to the metacarpals, using the method of Schuind.<sup>21</sup> Results showed the proportion of force transmitted through the radiocarpal joints for a healthy child was similar to those reported by Horii and Schuind, suggesting a sliding RBSM is appropriate for estimating the joint mechanics of the wrist. Also, results for JIA wrists were reasonable. The results of this study suggest that more force is transferred through the ulno-carpal joint in the JIA wrist than a normal wrist.

### **1.5.3 Multi-Body Contact Modeling**

Multi-body modeling is a powerful technique used to analyze complex structures involving rigid or deformable interacting bodies. Many multi-body modeling software programs have been developed which focus on various applications. Diarthrodial joints, being complex in nature, are not easily modeled with some commercial software, and require specific applications.

Kwak et al., developed a 3D multi-body contact algorithm modeling environment designed for analysis of the diarthrodial joints under quasi-static conditions.<sup>17</sup> Bones were modeled as rigid bodies with six degrees of freedom and the wrapping tendons or ligaments were modeled using imbedded particles with only three translational degrees of freedom. These particles in the tendons and ligaments were used to

redirect and transmit forces into the surfaces associated with the particle and the body around which the tendon or ligament was wrapping. A constant force was used to simulate muscle forces, applied along the linear direction which inserts on two bodies. Articular surfaces were modeled with triangle or quadrilateral patches. Surface contact link contact was modeled using a body-pair surface contact rule. The general algorithm and computer interface allowed for a variety of force-displacement ligament models as well as cartilage deformation models. In general, surface contact pressure at any point on the primary body was determined by penetration of that point into the surface of the contacting body. Newton-Raphson method was employed for a convergence solution algorithm. The algorithm and computer program was then used to model the patellofemoral joint of six cadaver knees. The kinematic transformations predicted were consistent (translation within 1 mm in x, y, and z planes, rotation within 2°) with experimental data. Thus, the approach was found to be adequately accurate and computationally efficient.

Pillai et al., developed a procedure to determine radiocarpal joint contact mechanics from MRI based models.<sup>20</sup> MRI images of four human subjects in grasp and relaxed positions were obtained using a 1.5 Tesla whole-body scanner with a flexible wrist coil. During the grasp sequence, subjects were asked to lightly grasp a cylinder and to maintain the same level of grasp during the scan. The second scan, with the hand relaxed, was then completed without repositioning the subject or reorienting the MRI scanner. MR images were manually segmented with custom software to produce contour stacks for each bone in the radiocarpal joint (radius,

lunate, and scaphoid) with and without cartilage for the relaxed image set, and without cartilage for the grasp image set. Kinematics of the bones from relaxed state to grasp state were determined by analysis of bone-only contours from each image set. Using the radius as a fixed reference, surface registration was used to determine the rotation and transformation vectors of the lunate and scaphoid bones between loaded and unloaded states. The kinematics were implemented into the Joint\_Model program developed at Columbia University,<sup>17</sup> along with the bone models. Cartilage thickness was assumed to be a uniform thickness of 1.0 mm on each bone, and a linear effective compressive modulus of 4.0 MPa was used. Results were consistent with other experimental data in literature.

Thoomukuntla et al.<sup>25</sup> began work validating the method developed by Pillai. Three cadaveric forearms were given a volar dissection of the wrist, for insertion of either static pressure-film or an electronic pressure sensor. Three flexor tendons (FDS, FDP, FPL) were isolated in the forearm so that loads could be applied to the arm, simulating grasp of the hand. The forearm was fixed to a base plate to hold the forearm in a neutral rotation. Then either of the sensors was inserted, and the loads were applied through the tendons. This procedure was repeated in an MRI scanner. Images were taken of the wrist bones in both relaxed and loaded states. Bone and cartilage models of the radius, scaphoid, and lunate bones were developed from the relaxed image set. Kinematic transformations were obtained by comparing using the radius as a reference and finding the attitude and rotation vector of the scaphoid and lunate from unloaded to loaded states. These kinematic transformations, along with

the bone models, were loaded into the Joint\_Model program. Results were encouraging. They found a correspondence between pressure data found using the pressure-sensitive sensor, film, and the MRI-based model. Also, bone contact areas were calculated directly from the MR images by mapping points along the contact in each image, finding the arc lengths between these points, and then taking the sum of the arc lengths multiplied by the slice thickness to get an area. By doing this for the whole image set, the total contact area was found. This data matched closely the contact areas reported by the MRI-based model. However, only three specimens were completed, and more work was needed to refine this method, as the experimental data was questionable.

Continuing work to validate this method is currently in progress, and is the topic of the work reported here.

#### **1.5.4 Development of Accurate Models from Images**

Computational modeling has the benefit of allowing non-invasive load-bearing simulation. These models help clinicians understand many conditions, like trauma from repetitive stress, degenerative diseases like OA, and acute injuries. Accurate models can provide surgeons and bioengineers with investigative tools to increase basic knowledge as well as improve treatment techniques.

Accurate representation of the human tissue is critical to exposing the mechanisms underlying disorders of the body. Replication of human anatomy is a complex process, but invariably begins with an image or image set. The most

common methods acquire images of bone, soft tissue, or a combination of both. These images are then used to create 2D or 3D models.

For 2D models, x-rays can sometimes be used, and are highly accurate and simple to acquire. For 3D models, CT and MRI represent the cutting edge of imaging techniques. CT allows for highly accurate models of bones (sub-millimeter resolution), but cannot image soft tissue near the bones accurately. MRI allows for high quality images of bone contours, as well as soft tissues such as cartilage. While MRI can view bone and soft tissues, it can suffer from a lack of contrast or a poor signal-to-noise ratio (SNR).

Classically, modeling from images occurs in three stages. The first step is segmentation. This involves extracting geometry (contours) for each structure of interest out of a single image. For CT, extraction usually is done automatically, using threshold-based methods. MRI contours are usually developed manually. Assembly is the next step, and involves combining these individual contours into a 3D point cloud. Lastly, surface mapping occurs. This is the development of a surface description based on the 3D point cloud, and may be the final product which is used in the biomechanical analysis (along with kinematic description), or the volume may be meshed for finite element analysis.

## **1.6 Validation Methods**

However accurate the kinematic or dynamic modeling technique appears to be, it is necessary to validate them using experimental data so that their feasibility and

accuracy for simulating joint mechanics can be analyzed. Several investigations have attempted to measure radiocarpal contact mechanics using experimental models.

While all the experiments have limitations, they provide useful data for comparison which can test the validity of modeling techniques.

### **1.6.1 Experiments Using Pressure Sensors in the Radiocarpal Joint**

Tencer et al. used Fuji pressure sensitive film to determine the pressure distribution properties of the normal radiocarpal joint.<sup>24</sup> The pressure sensitive film was inserted dorsally into the radiocarpal joint of a cadaver forearm and the specimen was tested in 36 positions combining flexion/tension with radioulnar deviation and supination/pronation. The overall thickness of the film was 0.28 mm, allowing it to conform to the contours of the articulating surface. The hand was positioned in a jig that allowed for loading in different positions. A load of 103 N was applied using dead weights across the second and third metacarpals. The pressure print obtained from loading was isolated into four zones based on color intensity saturation values. Results showed the overall joint pressure averaged 3.17 MPa for a load of 103 N over all joint positions tested.

Kazuki et al. measured the pressure distribution in the radiocarpal joint using pressure sensitive film.<sup>16</sup> They analyzed the pressure distribution in four cadaver wrists, two normal and two with simulated malunited Colles fracture. The specimens were mounted on a testing apparatus and 100 N was applied axially to the wrist through the third metacarpal. It was concluded that radiosaphoid and radiolunate

articulations had mean articular pressures of 2.8 and 2.7 MPa, respectively, in normal wrists. The contact locations moved from volar to dorsal in specimens with Colles fracture.

Anderson et al. tested the contact stress distributions in malreduced distal radius fractures using pressure sensitive film.<sup>1</sup> Twelve cadaver forearms were dissected, and Fuji pressure-sensitive film was inserted into the radiocarpal joint. Simple intra-articular fractures were created that allowed distal radius articular incongruity. It was determined that contact stress was significantly higher for the anatomically reduced radii than for the non-reduced specimens. However, contact stress elevation was only modest, which suggested other factors may be responsible for pathogenesis of radiocarpal OA in the presence of residual articular incongruity after fracture.

Hara et al. investigated the pressure distribution in the radiocarpal joint using a pressure sensitive rubber sensor.<sup>12</sup> The transducer used was thin, flexible, and capable of quasi-instantaneous measurements. It also had an advantage over pressure film; it could take multiple measurements without changing the loading configuration or replacing the sensor. The sensor was placed in the joint using a dorsal approach, without damaging the radiotriquetral ligament. The specimen was fixed to a custom-designed frame and a load of 0 to 12 kg was applied through seven tendons; five wrist motor tendons, the finger flexor tendons, and the flexor pollicis longus. Results showed that for a load of 10 kg, the peak pressure was 2.4 MPa in the scaphoid fossa and 1.5 MPa in the lunate fossa, and the peak pressure ratio between the scaphoid and lunate was 1.7 when the wrist was in neutral position. It was concluded that for 10 kg

of loading, force transmission was 50% through the scaphoid fossa, 30 - 35% through the lunate fossa and 10 - 15% through the triangular fibrocartilage complex (TFCC).

### **1.6.2 Validity of Using Pressurex Film or Tekscan Sensor**

While both static film and dynamic pressure sensors have been used to measure radiocarpal contact mechanics, it is important to understand the limitations of both these systems as a method of validating computation models.

Wilson et al. assessed the accuracy and repeatability of a Tekscan sensor.<sup>27</sup> Tekscan sensors are thin, piezoresistive matrices of sensels that provide real-time contact pressure. Known forces were applied to the sensor using a materials testing machine. Five trials at seven different loads were recorded. Results showed that the sensor was accurate to within 6.5%. The sensor was then tested in four cadaveric knees, and a variability of 9.1% was found. It was concluded that the dynamic pressure sensor could have accuracy and repeatability similar to Fuji pressure sensitive film.

A similar study conducted by Wilson et al. assessed the same sensor in the lumbar spine.<sup>28</sup> Five trials each were performed on four cadaveric specimens, with loads of 25, 50, and 100 N applied to the natural facet joint. Results showed force estimates were accurate to within 4-6%. However, using the two-point power curve calibration method included with the sensor software caused an overestimation of loads by as much as 56%. It was concluded that the sensor could be accurate, but measurement repeatability and accuracy was highly dependent on calibration protocol.

Harris et al. conducted a direct comparison of pressure sensitive film and a dynamic piezoelectric pressure sensor.<sup>13</sup> Harris analyzed the contact area between the femoral component and the tibial insert of a total knee arthroplasty (TKA) device. The TKA device was tested at angles of 0 to 110 degrees of flexion with loads equaling 4, 4.5 and 5 times body weight. Results showed the contact areas measured with Fuji pressure sensitive film was 11-36% lower than that measured by the dynamic pressure sensor, which was the more accurate method. Accuracy of force and pressure measurement was not a part of this study.

Similarly, Bachus analyzed the two sensor types, but in this case used a cylinder and base plate mounted on a materials testing machine.<sup>4</sup> Results did not support the hypothesis that all sensors would report loads within 5% of actual applied load, but similarly to Harris, it was found that the dynamic pressure sensor was more accurate than the pressure sensitive film. The Fuji film showed higher error than the Tekscan sensor in force measurement, with Fuji film having an error between 4-13%, and the Tekscan sensor overestimating loads by 2-3%. In pressure measurement, the Tekscan sensor was found to be much more accurate, with an average error of 3%, while the Fuji film had an average overestimation error of 23%.

Fregly et al. tested the discretization error of the Tekscan sensor in the patellofemoral joint.<sup>10</sup> Contact pressure measurements were taken on four total knee replacements to estimate the magnitude of discretization errors in practical situations. It was found that the predicted errors were on the order of 1-4% for contact force and

peak pressure and 3-9% for average pressure and contact area. These errors were comparable to truncating pressures with pressure sensitive film.

Drewniak tested the accuracy Tekscan sensors when using a circular indentors of several sizes.<sup>9</sup> Static loads from 1000 N to 7000 N were applied to four flat, circular indentors and the contact areas were recorded with two different Tekscan sensor models (4000 and 5076). It was found that the Tekscan sensors had an error of 5% to 27% depending on the load applied. A threshold filter was applied, and the average error was reduced to less than 1%. However, it was noted that this method, though applicable for flat, idealized indentors, may not work for more complex surfaces and shapes.

Although dynamic pressure sensors have shown a higher level of accuracy in prediction of joint loads and contact areas, current sensor resolution is at least an order of magnitude worse than the current resolution of pressure sensitive film, and as such the use of pressure sensitive film cannot be dismissed completely. In small, geometrically complex joints such as the human wrist, pressure sensitive film may reveal contact pressure that would go undetected by a dynamic pressure sensor.

### **1.6.3 Projected Cartilage Modeling**

A common technique in joint modeling is the use of artificial cartilage layers. Because high resolution images and high quality bone models can be created from x-ray images or CT imaging data, it is popular to build bone models from that data and then attempt to estimate the cartilage surfaces which surround some or all of the bone.

Ulrich et al., developed a 2D model for FEM load transfer analysis of the distal radius using high-resolution CT images.<sup>26</sup> Bones were directly modeled from the CT data, however cartilage surfaces were created by adding a 3 mm uniform layer to the bones. The uniform cartilage thickness was chosen from images found in literature, and did not necessarily match the cartilage thickness of the specimens being modeled. High strain energy values were found in the distal radius.

Anderson et al., created subject-specific models of the human ankle joint.<sup>3</sup> Ankles were imaged using CT, then segmented into models using custom-written Matlab code. Articular cartilage was projected a uniform thickness of 1.7 mm. The actual specimen cartilage thickness was not known, so this value was obtained from previous literature. The experimental pressure data showed a close match (3.2% error) with one of the two ankles tested, however the other ankle showed 19.2% error. This calls into question the validity of using a standardized cartilage thickness for different specimens.

Beek et al., created 3D model of the temporomandibular joint for FEM analysis.<sup>5</sup> Models of the bones were created by a magnetic tracking device tracing plaster molds of the actual bones. The bones were modeled as rigid bodies. Cartilage layers, as well as the TMJ disc, were then generated using finite element pre-processing software. Neither the thickness of the cartilage, the thickness of the TMJ disc, nor how either was obtained was stated. It was found that the displacement of the model closely matched the actual displacement of the specimen during bite with an applied load of

327 N. The usefulness of the kinematic results of this study is questionable, because there was little experimental data to which it could be compared.

Carrigan et al., created a 3D model of the wrist and used FEM to calculate carpal load transmission.<sup>7</sup> CT scans were used to create bone models of all the wrist bones as well as the distal radius and ulna. These models were meshed using finite element software. To create the cartilage surfaces on the bones, a 1.0 mm projection was implemented on the surface of each bone. This projection was created by directing a vector normal offset of 1.0 mm at each node. Models were tested using a 15 N compressive force to the capitate. It was found that cartilage material modulus (varied from 5 MPa to 10 MPa in this study) and kinematic constraints had substantial impact on the articular contact patterns and pressures. This study in particular highlights the importance of accurate cartilage mapping. If cartilage modulus has a significant impact on contact area, contact stress, and carpal rotation, then it highlights the need to model that cartilage as accurately as possible, given the direct relationship between a material's thickness, and its strain.

## 1.7 References

1. Anderson DD, Bell AL, Gaffney MB, Imbriglia JE. Contact stress distributions in malreduced intraarticular distal radius fractures. *J Orthop Trauma* 1996;10(5):331-7.
2. Anderson DD, Daniel TE. A contact-coupled finite element analysis of the radiocarpal joint. *Semin Arthroplasty* 1995;6(1):30-6.
3. Anderson DD, Goldsworthy JK, Li W, James Rudert M, Tochigi Y, Brown TD. Physical validation of a patient-specific contact finite element model of the ankle. *J Biomech* 2007;40(8):1662-9.
4. Bachus KN, DeMarco AL, Judd KT, Horwitz DS, Brodke DS. Measuring contact area, force, and pressure for bioengineering applications: using Fuji Film and TekScan systems. *Med Eng Phys* 2006;28(5):483-8.
5. Beek M, Koolstra JH, van Ruijven LJ, van Eijden TM. Three-dimensional finite element analysis of the cartilaginous structures in the human temporomandibular joint. *J Dent Res* 2001;80(10):1913-8.
6. Buckwalter JA, Saltzman C, Brown T. The impact of osteoarthritis: implications for research. *Clin Orthop Relat Res* 2004(427 Suppl):S6-15.
7. Carrigan SD, Whiteside RA, Pichora DR, Small CF. Development of a three-dimensional finite element model for carpal load transmission in a static neutral posture. *Ann Biomed Eng* 2003;31(6):718-25.

8. DiDonna ML, Kiefhaber TR, Stern PJ. Proximal row carpectomy: study with a minimum of ten years of follow-up. *J Bone Joint Surg Am* 2004;86-A(11):2359-65.
9. Drewniak EI, Crisco JJ, Spenciner DB, Fleming BC. Accuracy of circular contact area measurements with thin-film pressure sensors. *J Biomech* 2007.
10. Fregly BJ, Sawyer WG. Estimation of discretization errors in contact pressure measurements. *J Biomech* 2003;36(4):609-13.
11. Garcia-Elias M, An KN, Cooney WP, Linscheid RL, Chao EY. Transverse stability of the carpus. An analytical study. *J Orthop Res* 1989;7(5):738-43.
12. Hara T, Horii E, An KN, Cooney WP, Linscheid RL, Chao EY. Force distribution across wrist joint: application of pressure-sensitive conductive rubber. *J Hand Surg [Am]* 1992;17(2):339-47.
13. Harris ML, Morberg P, Bruce WJ, Walsh WR. An improved method for measuring tibiofemoral contact areas in total knee arthroplasty: a comparison of K-scan sensor and Fuji film. *J Biomech* 1999;32(9):951-8.
14. Horii E, Garcia-Elias M, Bishop AT, Cooney WP, Linscheid RL, Chao EY. Effect on force transmission across the carpus in procedures used to treat Kienbock's disease. *J Hand Surg [Am]* 1990;15(3):393-400.
15. Iwasaki N, Genda E, Minami A, Kaneda K, Chao EY. Force transmission through the wrist joint in Kienbock's disease: a two-dimensional theoretical study. *J Hand Surg [Am]* 1998;23(3):415-24.

16. Kazuki K, Kusunoki M, Shimazu A. Pressure distribution in the radiocarpal joint measured with a densitometer designed for pressure-sensitive film. *J Hand Surg [Am]* 1991;16(3):401-8.
17. Kwak SD, Blankevoort L, Ateshian GA. A Mathematical Formulation for 3D Quasi-Static Multibody Models of Diarthrodial Joints. *Comput Methods Biomech Biomed Engin* 2000;3(1):41-64.
18. Ledoux P, Lamblin D, Targowski R. Modifications to the mechanical behavior of the wrist after fracture of the scaphoid. Modeling by finite element analysis. *Acta Orthop Belg* 2001;67(3):236-41.
19. Manal K, Lu X, Nieuwenhuis MK, Helders PJ, Buchanan TS. Force transmission through the juvenile idiopathic arthritic wrist: a novel approach using a sliding rigid body spring model. *J Biomech* 2002;35(1):125-33.
20. Pillai RR, Thoomukuntla B, Ateshian GA, Fischer KJ. MRI-based modeling for evaluation of in vivo contact mechanics in the human wrist during active light grasp. *J Biomech* 2007.
21. Praemer, A. K. et al., Biomechanics of the distal radioulnar joint. American Academy of Orthopaedic Surgeons, Rosemont IL, 1999
22. Rettig ME, Raskin KB. Acute fractures of the distal radius. *Hand Clin* 2000;16(3):405-15, ix.
23. Schuind F, Cooney WP, Linscheid RL, An KN, Chao EY. Force and pressure transmission through the normal wrist. A theoretical two-dimensional study in the posteroanterior plane. *J Biomech* 1995;28(5):587-601.

24. Tencer AF, Viegas SF, Cantrell J, Chang M, Clegg P, Hicks C, O'Meara C, Williamson JB. Pressure distribution in the wrist joint. *J Orthop Res* 1988;6(4):509-17.
25. Thoomukuntla, B.R., (2005) Master's Thesis: Preliminary Validation of MRI-Based Modeling for Joint Contact Mechanics. Mechanical Engineering, University of Kansas
26. Ulrich D, van Rietbergen B, Laib A, Ruegsegger P. Load transfer analysis of the distal radius from in-vivo high-resolution CT-imaging. *J Biomech* 1999;32(8):821-8.
27. Wilson DC, Niosi CA, Zhu QA, Oxland TR, Wilson DR. Accuracy and repeatability of a new method for measuring facet loads in the lumbar spine. *J Biomech* 2006;39(2):348-53.
28. Wilson DR, Apreleva MV, Eichler MJ, Harrold FR. Accuracy and repeatability of a pressure measurement system in the patellofemoral joint. *J Biomech* 2003;36(12):1909-15.

## **Chapter 2. Accuracy and Repeatability of Piezoresistive Sensor and Pressure Sensitive Film in the Radiocarpal Joint**

### **Abstract**

The purpose of this study was to analyze the accuracy of both the Tekscan I-Scan system and Pressurex film for use in radiocarpal joint pressure distribution measurements. Six sets of idealized accuracy tests were performed in a servohydraulic testing machine, first creating a 10-point calibration with constant pressures for each test set, then testing two cylindrical objects. The Tekscan calibration data was converted from raw values into a quadratic regression curve. The Pressurex film was scanned into a digital image file and analyzed to create a cubic regression curve. Calibrations were used to predict loads created by two cylindrical objects. It was determined that the Tekscan system generally predicts loads within 10% of actual, and was the more accurate of the two methods. Finally, an *in situ* test was performed on a human cadaver wrist using the Tekscan sensor. A calibration was performed, then a different set of loads were applied. The predicted loads from the Tekscan system were used to test the accuracy of the sensor in the joint. The Tekscan sensor performed with a similar degree of accuracy and repeatability in the *in situ* test as in the idealized control tests. The Tekscan sensor appears to be somewhat more accurate for load measurement than Pressurex film and is more robust for measurements in joints.

## 2.1. Introduction

Various techniques to analyze the kinematics, and joint forces in the wrist (and other joints) have been developed. They fall under two major categories: sensor experiments and computational modeling.<sup>1,9</sup> Sensor experiments refer to sensing devices or materials directly introduced into the joint space to measure pressure distribution, contact areas, and force transmission. Computational models refers to any numerical model used to predict the contact, forces, and motion of the bones in the joint.

By far the most popular method of creating the computational model geometry is from CT (computed tomography) scan data.<sup>6,7</sup> Because of the relatively high resolution of CT scans, a very accurate 3D model of the bones of the wrist can be developed, and relatively easily. However, CT imaging does not show soft tissue, so for joint modeling, the cartilage surface is generally projected from the bone surface. Even model geometry, generated from MRI data, with accurate cartilage surfaces needs accurate boundary conditions, and establishing *in vivo* boundary conditions can be problematic. Still, these techniques are useful in many situations, and they can provide insightful data.

Several methods have been developed for analyzing joint mechanics: rigid-body spring models,<sup>3</sup> finite-element modeling (projecting meshes),<sup>4,5</sup> and surface contact models.<sup>11</sup> All of these techniques have limitations on their application and accuracy.

Sensor experiments rely on the ability to dissect the joint and insert a measurement device. Thus this approach is generally not acceptable in human

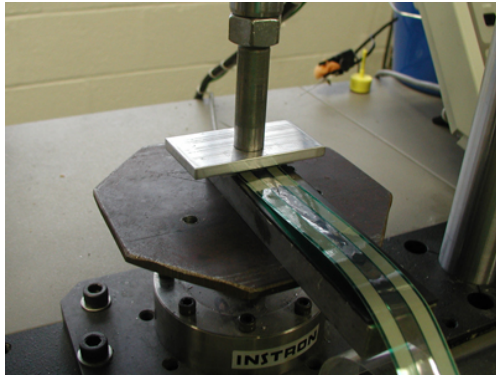
subjects experiments. Piezoresistive and piezoconductive sensors have been used, as well as pressure sensitive film.<sup>2, 8, 10, 12, 14, 15</sup> Tekscan makes piezoresistive sensors for use in *in situ* joint testing, and those sensors have been studied in the spine, knee and ankle joints in some detail.<sup>2, 14, 15</sup> Pressurex makes a variety of pressure sensitive films, for use in many different applications, from the automotive industry to podiatry. The Tekscan sensors also vary considerably. This study sought to compare the Tekscan #4201 sensor, which is designed for use in the wrist, and Pressurex Super-Low film, which has the best measurement range for pressures in the radiocarpal joint. We hypothesized that the Pressurex film would yield more accurate data, because of its higher spatial resolution.

## **2.2. Materials and Methods**

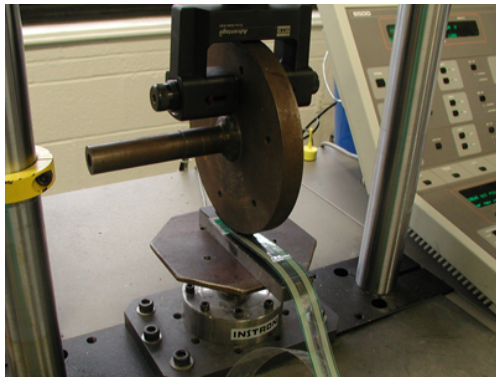
### **2.2.1 Idealized Tests**

Six sets of idealized tests were conducted. The idealized tests were performed with a servohydraulic materials testing machine (Instron 8511, Instron Corp., Canton, MA) equipped with a 10.0 kN electronically calibrated load cell. In each accuracy test, a regression curve was created using 10-points in 100 N increments from 100 N to 1000 N. The Pressurex calibration used a flat, 15.9 mm diameter circular indenter (area 200 mm<sup>2</sup>) covered with 1.6 mm thick 80A durometer rubber (Fig. 2.1a). The base upon which the film being tested was placed was also covered with 80A rubber of equal thickness. The Tekscan sensor was calibrated between the base rubber and a 15 mm X 15 mm piece of rubber, backed by an aluminum plate. The rubber sheets

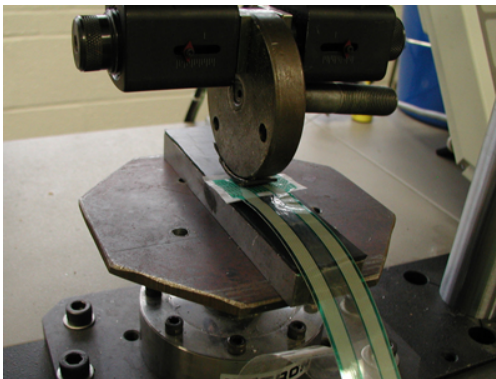
simulated cartilage and protected the film and sensor from the sharp contact of metal edges. Each load was applied using load control, then released, and a new section of the base was used for the next load so that minimal pre-compression of the rubber would occur during tests. After calibration, loads were applied with two cylindrical objects that also had a 1.6 mm layer of 80A durometer rubber (Fig. 2.1b, 2.1c).



(a)



(b)



(c)

**Figure 2.1.** Experimental setup used in this study (Tekscan setup shown here). Calibration of the sensor (a), larger radius object (b) and smaller radius object (c).

The larger object (obj.1) had a radius of 152.4 mm and the smaller object (obj. 2) had a radius of 76.2 mm. Loads were applied at 100 N increments from 100 N to 700 N. Because of the decreased contact area and subsequent increase in peak pressure, it was determined that higher loads would be more likely to create pressures outside the normal loading of the wrist and the measurement range of the Pressurex film. The purpose of testing these objects was to provide a non-uniform loading profile to determine the extent to which the measurement systems could predict loads applied with non-uniform pressure distributions. The calibration was performed and both objects were tested in immediate succession, to assure similar temperature and humidity throughout the process, as these environmental parameters can affect both the Tekscan sensor and Pressurex film. Each accuracy test was performed on a different day, as a way of better quantifying the normal variability of the data.

### **2.2.2 Tekscan Data Collection**

Because of the unique geometry of the joint, Tekscan sensor 4201 (Tekscan, South Boston, MA) was used. This sensor is specifically designed for use in the radiocarpal-ulnocarpal joint. For the Tekscan data in each accuracy test, raw values and contact areas were taken from the I-Scan software (rev. 5.1) provided with the Tekscan system, and analyzed in Microsoft Excel. For the 10-point calibration,

average pressures ranged from 0.45 – 4.5 MPa. By comparing the average raw value (for each load) versus pressure (obtained by dividing the known applied force by the contact area reported from the Tekscan sensor), a quadratic, regression equation was obtained (Fig. 2.2). Each cylindrical object was then tested. Raw data was captured for each sensel of the sensor (Fig. 2.3 a,b). The raw value for each sensel was then converted into a pressure, and multiplied by the known area of the sensel to create a force. By summing these individual sensel forces, it was possible to compare the total measured force against the load applied by the Instron system.

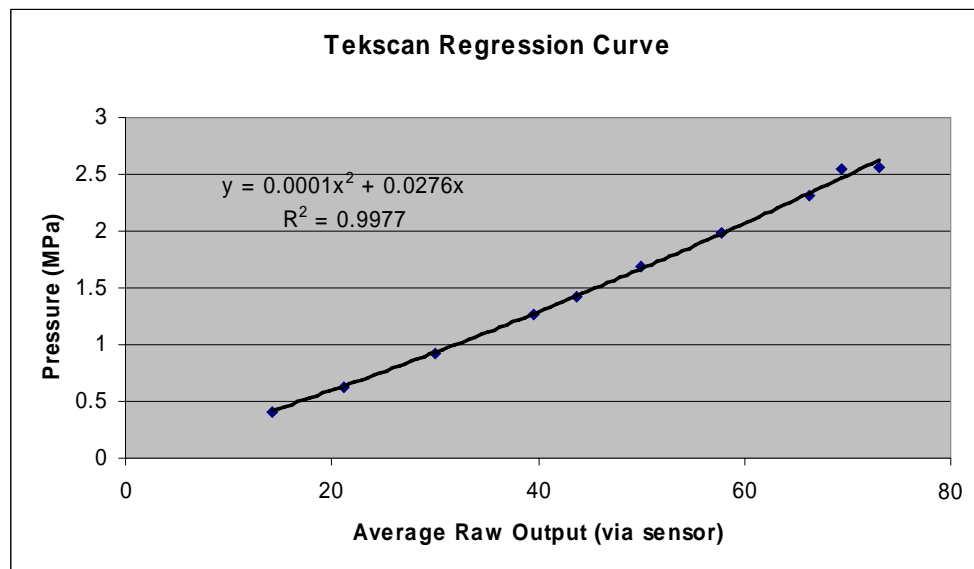


**Figure 2.2.** Typical regression equation, curve, and coefficients developed from Tekscan output data (Test 1 curve shown here).

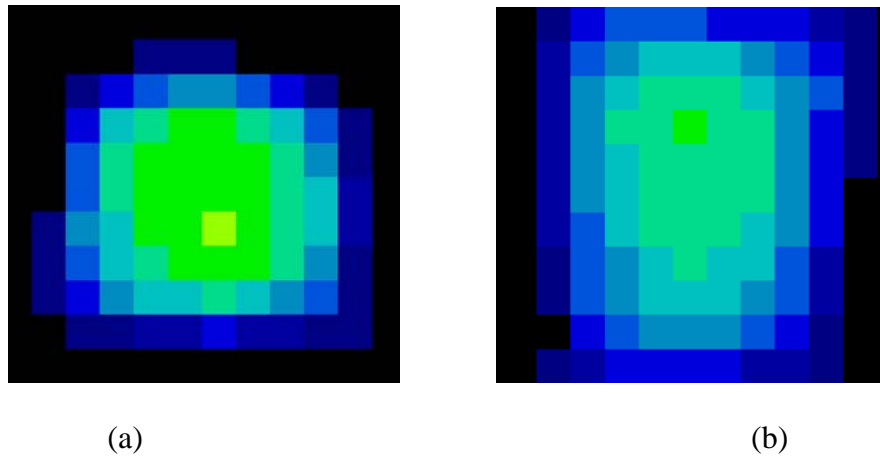


**Figure 2.3.** Raw Tekscan image from cylindrical object tests (700N). (a) Smaller radius object and (b) Larger radius object.

### 2.2.3 Pressurex Data Collection

For the next portion of the experiment, Pressurex Super-Low film was chosen. This film has an ideal pressure range of 0.5-2.5 MPa, which is well suited for simulating normal wrist loading. Similar to the Tekscan tests, a 10-point calibration was created using loads of 100 N to 1000 N in 100 N increments (pressures from about 0.5 - 5.0 MPa).

To capture this data, the film was scanned (Epson Perfection 3490, Epson, Long Beach, CA) at a resolution of 72 dpi. Because Pressurex is not a continuous color distribution, scanning at very high resolutions can result in artificially high peak pressures. Therefore 72 dpi was found to be an acceptable resolution to reduce noise and transfer the film image into a usable image file for analysis. The images were then analyzed in Adobe Photoshop (ver. 6.0.1, Adobe Systems Inc, San Jose, CA). In Photoshop, it was possible to obtain the red, green, and blue intensity value for each

pixel. For calibration, the average was calculated and entered into Microsoft Excel. In Microsoft Excel, it was possible to calculate the normalized red and normalized blue values. Normalized red refers to the red intensity divided by the sum of the red, blue, and green intensity for a particular load. Similarly, normalized blue is simply the blue intensity divided by the sum of all three intensities. Finally, normalized red minus normalized blue was calculated, and then compared to the pressure of that particular load. The pressure was found by dividing the applied force (input into the Instron system) by the area of the film stained. This “normalized difference” versus pressure enabled the development of a cubic regression curve with reasonable accuracy (Fig. 2.4).<sup>13</sup>

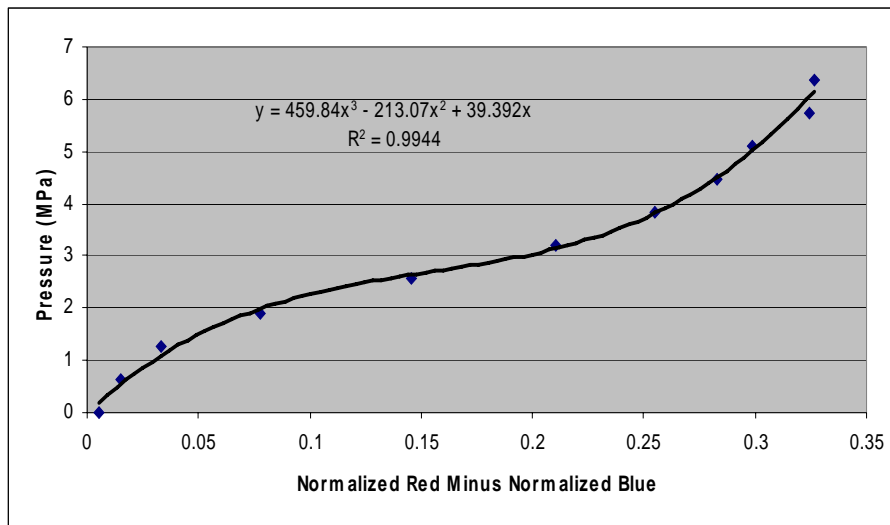


**Figure 2.4.** Typical regression curve developed from Pressurex data (Test 1 curve shown here).

Next the two cylindrical objects were tested. These were tested in an identical manner as when tested with the Tekscan sensor. After data collection, these impressions were also scanned at 72 dpi and analyzed in Photoshop. The difference between normalized red and normalized blue was then found, as was the impression area. Using these data, and the regression curve from the calibration, it was possible to find the measured force, and compare it to the applied force.

#### **2.2.4 *In Situ* Testing**

The final test performed was an *in situ* test of the Tekscan sensor in a human cadaveric wrist using an MTS servohydraulic testing machine (Model 858, Eden Prairie, MN). A human forearm was dissected and the second through fifth carpal bones were isolated and potted. The humerus was also isolated and potted. The whole arm was positioned in custom fixtures that held the metacarpal bones and humerus in such a way as to hold the wrist in a neutral position with respect to flexion-extension, radioulnar deviation, and forearm rotation (Fig. 2.5). The wrist was dissected volarly for insertion of the Tekscan sensor.

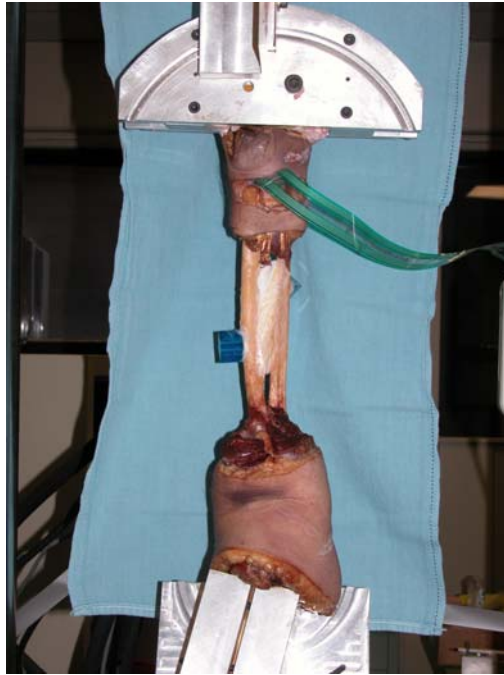


**Figure 2.5.** Experimental setup for *in situ* test of Tekscan sensor. Here the forearm is shown with the Tekscan sensor inserted in the ulnocarpal & radiocarpal joints (the dissection of the radius and ulna was for an independent study unrelated to this manuscript).

The specimen was subjected to loads in 50N increments, from 50 N to 250 N, to create a 5-point calibration curve. This allowed the development of a quadratic regression curve following the same procedure as in the idealized tests. Loads were then applied from 25N to 225N at 50N increments, and were used as the experimental values. These raw sensor values were used to obtain a measured force which could be compared to the applied force.

## **2.3. Results**

### **2.3.1 Tekscan**

The Tekscan sensor showed good repeatability. The average forces measured for any set of tests were at worst within 17.0 (4.0) % of actual (Table 2.1a). The overall average percent error over the whole range of tests of both cylindrical objects was 7.2 (5.3) %. The larger cylindrical object was generally more accurate, with an average error of 5.6 (4.3) %, as opposed to the 8.8 (6.3) % error for the smaller radiused object. It was found that 80% of errors fell within 11.1% error and that 95% of errors fell within 17.1% of the applied load.

### **2.3.2 Pressurex**

The normalized red minus normalized blue method at 72 dpi proved to be a reliable and accurate method for obtaining repeatable measures, as has been suggested by other investigators.<sup>13</sup> The Pressurex film (Table 2.1b) had similar, but higher, variability with higher average errors than the Tekscan sensor. Average force error for the larger cylindrical object was 16.0 (15.7) %, and 11.5 (10.4) % for the smaller object. The largest average error from a single set of tests was 21.6 (20.9) %. The overall average percent error over the whole range of testing was 13.8 (13.1) %. It was found that 80% of errors fell within 17.9% and 95% of errors fell within 21.5% of the applied load.

**Table 2.1.** Results of (a) Tekscan and (b) Pressurex tests. Standard deviations are in parentheses. The average standard deviation refers to the standard deviation of all data points from all tests.

	Average Errors (%)			Average Errors (%)	
	Obj. 1	Obj. 2		Obj. 1	Obj. 2
<b>Test 1</b>	11.1 (4.3)	17.0 (4.0)	<b>Test 1</b>	17.5 (23.3)	15.3 (7.3)
<b>Test 2</b>	3.8 (3.1)	4.8 (3.1)	<b>Test 2</b>	19.8 (10.9)	12.5 (16.2)
<b>Test 3</b>	4.4 (6.0)	15.6 (13.7)	<b>Test 3</b>	17.9 (24.6)	5.5 (9.8)
<b>Test 4</b>	2.4 (1.2)	3.5 (2.3)	<b>Test 4</b>	3.7 (4.8)	7.5 (5.3)
<b>Test 5</b>	3.1 (5.1)	7.1 (8.6)	<b>Test 5</b>	15.3 (9.5)	14.1 (8.7)
<b>Test 6</b>	8.6 (6.2)	4.9 (5.9)	<b>Test 6</b>	21.6 (20.9)	14.3 (15.4)
<b>AVG</b>	<b>5.6 (4.3)</b>	<b>8.8 (6.27)</b>	<b>AVG</b>	<b>16.0 (15.7)</b>	<b>11.5 (10.4)</b>

(a) (b)

### 2.3.3 *In Situ* Testing

The *in situ* tests showed the Tekscan sensor works at a similar level of accuracy in the joint as in the idealized tests. The *in situ* calibration curve and test results yielded an overall error of 5.6 (4.1) %, remarkably close to the error from the idealized Tekscan tests. All three main wrist joint articulations (radioscaphoid, radiolunar, ulnocarpal) can be clearly seen (Fig. 2.6) using the Tekscan sensor.

A further test was done, to determine the efficacy of the an idealized calibration on *in situ* testing. The sensor used for the *in situ* experiment was calibrated using the 10-point calibration technique described above, and a regression equation was obtained. The *in situ* data was then compared using this idealized calibration

equation. The forces predicted were interestingly less accurate, but more repeatable. The average force error was an underestimation of 8.0 (1.4) %. The greatest single error was at the applied load of 225N, where the error was 11.3%.

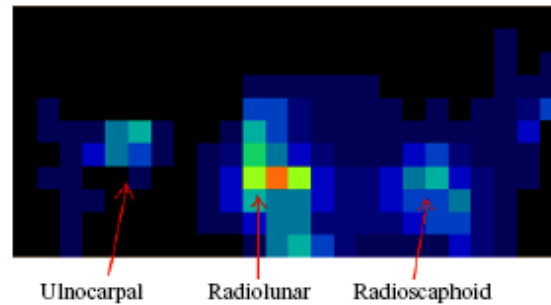


**Figure 2.6.** Sample (250N) result from Tekscan *in situ* test.

## 2.4. Discussion

This study tested the accuracy of both the Tekscan sensor (4201) and Pressurex Super-Low film for use in the radiocarpal joint. Knowledge of the accuracy and consistency of data from these systems is important for making conclusions about the practicality of these two systems for use in measuring pressures and forces in complex joints.

The results from both the Tekscan sensor and Pressurex film indicate that both methods are reasonably accurate and repeatable for gross estimates of forces in radiocarpal joint testing. However, neither system was capable of producing an average error less than 15% in 95% of tests. Therefore, these systems should not be used where highly accurate data is required.

The highest errors in the Tekscan sensor occurred during the first test. Errors were likely reduced in subsequent tests because of improved technique as the testing progressed. The Tekscan sensor measurement may also be considered more reliable than the Pressurex film because of the Tekscan sensor's tendency to consistently have positive (overestimation) error. The Pressurex sensor errors were less predictable and it often had negative errors at low loads, and positive errors at high loads. The consistently higher Tekscan measures could allow for a possible correction to be made during actual testing that may increase the accuracy of the predicted load. While shear forces can induce artifact in both systems, this is not very likely for these tests.

Part of the higher error in the Pressurex tests may be attributed to film artifact, which caused relatively high errors at low loads (100-200N), but became less of an issue at higher loads (500-700N). Because Super-Low film was used, extreme caution was necessary during handling; mild contact between the film and developer sheets could cause artifact. Because of these issues, the dynamic sensing capabilities of the Tekscan sensor may be preferable. However, the high resolution of the Pressurex film could potentially give more accurate pressure data under some loading conditions, such as in joint spaces where surface contacts are small enough that the higher resolution is very important.

## 2.5 References

1. Anderson DD, Daniel TE. A contact-coupled finite element analysis of the radiocarpal joint. *Semin Arthroplasty* 1995;6(1):30-6.
2. Anderson DD, Goldsworthy JK, Li W, James Rudert M, Tochigi Y, Brown TD. Physical validation of a patient-specific contact finite element model of the ankle. *J Biomech* 2007;40(8):1662-9.
3. Andriacchi TP, Mundermann A, Smith RL, Alexander EJ, Dyrby CO, Koo S. A framework for the in vivo pathomechanics of osteoarthritis at the knee. *Ann Biomed Eng* 2004;32(3):447-57.
4. Carrigan SD, Whiteside RA, Pichora DR, Small CF. Development of a three-dimensional finite element model for carpal load transmission in a static neutral posture. *Ann Biomed Eng* 2003;31(6):718-25.
5. Castano MC, Zapata U, Pedroza A, Jaramillo JD, Roldan S. Creation of a three-dimensional model of the mandible and the TMJ in vivo by means of the finite element method. *Int J Comput Dent* 2002;5(2-3):87-99.
6. Crisco JJ, McGovern RD, Wolfe SW. Noninvasive technique for measuring in vivo three-dimensional carpal bone kinematics. *J Orthop Res* 1999;17(1):96-100.
7. Fischer KJ, Manson TT, Pfaeffle HJ, Tomaino MM, Woo SL. A method for measuring joint kinematics designed for accurate registration of kinematic data to models constructed from CT data. *J Biomech* 2001;34(3):377-83.

8. Harris ML, Morberg P, Bruce WJ, Walsh WR. An improved method for measuring tibiofemoral contact areas in total knee arthroplasty: a comparison of K-scan sensor and Fuji film. *J Biomech* 1999;32(9):951-8.
9. Ishii S, Palmer AK, Werner FW, Short WH, Fortino MD. Pressure distribution in the distal radioulnar joint. *J Hand Surg [Am]* 1998;23(5):909-13.
10. Kazuki K, Kusunoki M, Shimazu A. Pressure distribution in the radiocarpal joint measured with a densitometer designed for pressure-sensitive film. *J Hand Surg [Am]* 1991;16(3):401-8.
11. Kwak SD, Blankevoort L, Ateshian GA. A Mathematical Formulation for 3D Quasi-Static Multibody Models of Diarthrodial Joints. *Comput Methods Biomech Biomed Engin* 2000;3(1):41-64.
12. Martinelli L, Hurschler C, Rosenbaum D. Comparison of capacitive versus resistive joint contact stress sensors. *Clin Orthop Relat Res* 2006;447:214-20.
13. Ng TW, Yeong WK. Inexpensive color evaluation of dye-based pressure-sensitive films for plantar studies. *J Biomech* 2005;38(10):2130-3.
14. Wilson DC, Niosi CA, Zhu QA, Oxland TR, Wilson DR. Accuracy and repeatability of a new method for measuring facet loads in the lumbar spine. *J Biomech* 2006;39(2):348-53.
15. Wilson DR, Apreleva MV, Eichler MJ, Harrold FR. Accuracy and repeatability of a pressure measurement system in the patellofemoral joint. *J Biomech* 2003;36(12):1909-15.

## **Chapter 3 Segmented Cartilage Models Versus Cartilage Models**

### **Projected from Bones**

#### **Abstract**

The purpose of this study was to determine the accuracy of projected cartilage models by comparing them to segmented cartilage models and experimental data collected from the Tekscan pressure sensor. The radiocarpal joint was dissected to allow the insertion of a pressure sensor. The forearm bones (radius and ulna) of three cadaveric specimens were dissected, and secured to a plastic loading apparatus. The flexor digitorum profundus, flexor digitorum superficialis, and flexor poccilus longus were isolated and used to simulate grasp and load the wrist. Loads of 50N, 30N and 30N were applied to each, respectively. The radiocarpal joint was dissected and measurements of joint contact forces were made using a Tekscan pressure sensor. MR images of the wrist were then captured in loaded and unloaded states. These images were segmented for the construction of three-dimensional models to represent the radius, scaphoid, and lunate bones. Segmentation for one set of models included cartilage. Segmentation for the other set of models included bone only, and the cartilage surfaces were projected outward from the bone surface a distance of 1 mm. This produced a uniform layer of simulated cartilage. Both sets of models were analyzed for pressure, force and contact area measurements using the Joint\_Model program, and compared to the experimental Tekscan data.

The two cartilage models had similar geometries, however the projected cartilage models had significant overestimation of contact pressure when compared to the

segmented cartilage models (and the Tekscan results). The overestimation was not consistent from specimen to specimen, making it difficult to develop a correction factor to address the possible errors from projected cartilage modeling.

### 3.1. Introduction

It is critical to develop the most accurate geometric model of the joint as possible. Advances in imaging technology, coupled with faster computational capabilities have revolutionized joint model simulation. However, limitations still exist. If x-ray or computed tomography (CT) imaging is used, it is often difficult to distinguish soft tissues, and only the bones are modeled directly from the images. The soft tissues are created later. Magnetic resonance imaging (MRI) represents another option. Because MR images reveal soft tissues, it is possible to directly segment cartilage layers when developing joint models.

Several methods have been developed to model joint mechanics. Finite element method (FEM) has gained popularity as increasing computational speed has allowed more complex models to be created and analyzed.<sup>1, 3, 7, 12, 17, 18, 20, 21, 23</sup> These models often create highly accurate representations of the bones. If the model is being used to study contact forces and mechanics, a cartilage layer is often projected from the bone surface, at a uniform height determined by the researcher.<sup>2, 4, 5, 6, 8, 9, 15</sup>

Rigid body spring models (RBSM) are also used. Like FEM models, these models create accurate depictions of bones, however they simulate articular surfaces as finite sets of compression springs.<sup>10, 11, 13, 14, 19, 24, 26</sup> Cartilage on one or both bones in contact can be modeled this way, and the spring properties are defined based on the cartilage of the joint. Tendons and ligaments can also be modeled as tensile springs, if whole joint mechanics are being analyzed. These RBSM models benefit from ease of development and computational efficiency compared to FEM models.

A third method is multi-body contact modeling. Often, the joint of interest is modeled as quasi-static, in that the boundary conditions are defined as fixed for a given configuration at a specific point in time. Contact mechanics are calculated based on the inter-penetration depth of the bodies and the defined contact rule.<sup>16, 22</sup> There exist several multi-body software programs which focus on this technique (ADAMS, DADS, Working Model, DYNAMAN, Articulated Total Body Model, etc.). Surface contact models maintain the computational efficiency of RBSM, but have continuous surfaces and more robust and flexible contact rules.

Whichever technique is used, the development of the cartilage layers on contacting bones must be done with care. Many investigations simply “project” the cartilage layer; a uniform, normal layer of cartilage is projected from the surface of the bone a prescribed distance.<sup>2, 4, 5, 6, 8, 9, 15</sup>

The purpose of this study was to determine the differences in measured joint contact force, contact area, and peak pressure in the radiocarpal joints when projected cartilage is created as opposed to cartilage surfaces directly segmented from MRI data.

## **3.2. Materials and Methods**

### **3.2.1 Wrist Preparation**

For this experiment, 3 human cadaveric forearms were used. The dissection of the specimen was performed in two steps. First, the soft tissues were removed from the radius and ulna in the mid-forearm. Care was taken to isolate and preserve the distal

section of the flexor digitorum profundus (FDP), the flexor digitorum superficialis (FDS), and the flexor pollicis longus (FPL) tendons for later use. The cadaveric wrist was then volarly dissected to expose and open the radiocarpal joint for insertion of the pressure sensor. Care was taken to avoid damage to bone surfaces within the joint. After dissection of the wrist, two 6.35mm diameter holes were drilled through the radius, and one through the ulna, to attach the specimen to a fixture plate. The holes were drilled such that the forearm was aligned in a neutral rotation. The plate upon which the forearm was mounted was then attached through additional plates to a pulley assembly. The pulley assembly allowed the application of tendon forces to the FDP, FDS, and FPL using suture loops, nylon lines, and weights (Fig. 3.1). All materials were plastic, so that the experimental setup could be used in conjunction with an MRI scanner without inducing artifact. Finally, the hand was taped to the baseplate, so that the wrist would remain in neutral position and not flex during loading.

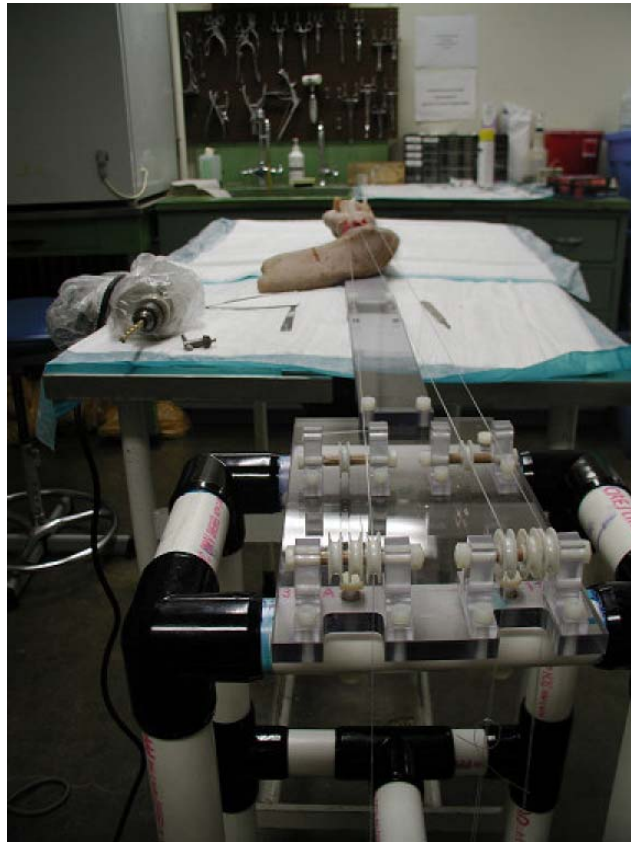


**Figure 3.1.** Attachment of forearm to pulley plate assembly

### 3.2.2 Tekscan Tests

A Tekscan (Tekscan Inc., South Boston, MA) pressure sensor was used for baseline testing. Tekscan sensors are thin, flexible, resistive sensors that use patterns of piezoresistive electrical conductors to produce a grid of sensing elements over which force distribution is measured. In this experiment Tekscan sensor #4201 was used, as it was specifically designed to fit in the radiocarpal joint. This sensor consists of a 24 X 11 grid of sensels with 8-bit resolution and a spatial resolution of 3.7 mm<sup>2</sup>. Data from the sensor was acquired by Tekscan I-Scan software (ver. 5.1).

The sensor was calibrated using a materials testing machine (Model #5811, Instron Corp., Canton, MA). Calibration utilized the Tekscan 2 point calibration procedure provided in the software. To do this, the sensor was placed between two plates with 1.6 mm, 70-durometer, adhesive-backed squares of rubber attached to them. The Instron machine applied a prescribed compressive force to the plates. A load of 220 N was applied for 10 seconds, followed by a higher load of 476 N for 10 seconds. This allows the software to develop a power curve calibration for application to the testing of the radiocarpal joint.

In order to get the sensor deep enough into the joint for accurate loading, we trimmed 2 mm off each side (radial and ulnar) of the sensor. Then it was wrapped in a thin plastic film to prevent cadaveric fluids from contaminating or damaging the sensor. The sensor was then inserted into the radiocarpal joint such that it covered both the radioscaphoid and radiolunate fossa. Loads of 50N, 30N and 30N were applied to the FDP, FDS, and FPL, respectively. Data was captured as soon as the load was stable (Fig. 3.2). This data was stored in the software as snapshots of raw data, which can be analyzed through the calibration in real-time or post-processed later.

Using the recorded raw data and the calibration file provided by the I-Scan software, it was possible to determine force, pressure and contact area. These values were used for comparison against the MRI-based model.

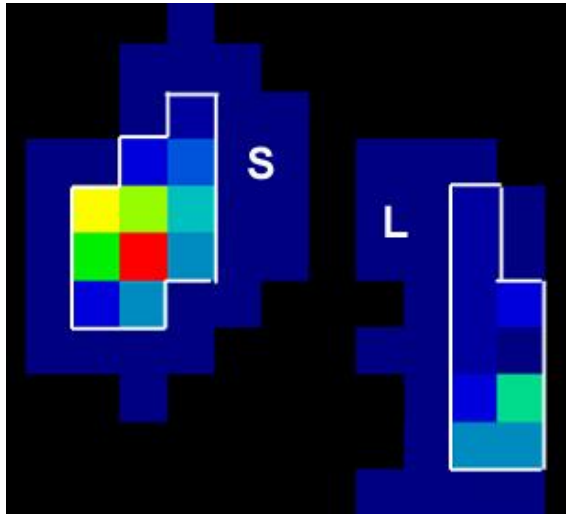


**Figure 3.2.** Sample Data from Tekscan Sensor (in situ). S indicates radioscapoid contact; L indicates radiolunate contact.

### 3.2.3 MRI Data Acquisition

MR Images for this study were acquired using a 9.4 Tesla (Unity INOVA Animal Systems, Varian Inc., Palo Alto, CA) research scanner using a T1 weighted spin echo sequence (TR 800, TE 5.13, Flip 45°). Scans were performed in the frontal plane with a field of view of 60 mm x 60 mm, with a resolution of 512x512 and a slice thickness of 1 mm. A total of 31 slices were included in the scan volume of each specimen.

Two sets of images were obtained for each specimen – relaxed and grasp. Relaxed images were taken with no applied loads to the three isolated tendons. Grasp images were taken with 50N, 30N and 30N applied to the FDP, FDS, and FPS, respectively. During application of this load, a piece of PVC pipe (42 mm outside

diameter) was placed in the hand as an object to grasp. The image data was captured and transferred to a research computer for analysis.

### **3.2.4 Computer Modeling**

The MRI images were segmented using the custom in-house software MPX\_Image (Ted Manson, 1998, University of Pittsburgh). To build bone contours for the radius, scaphoid and lunate, manual segmentation was performed with Bezier spline superimposition on the images of the bones. The contour data could then be saved as a text (\*.txt) file which contained the coordinates of points within the splines. This contour data was imported into PEd (Damion Shelton, 2000, University of Pittsburgh) to assemble three-dimensional contours (Fig. 3.3). The contours were then exported in a file format that could be read by the Nuages program (Bernhard Geiger, 1993, France). This software creates surface geometry using Delauney triangulation. The surface geometry file was converted using custom programs to the file format for use in the Joint\_Model program (Kwak et al., 2000, Columbia University).

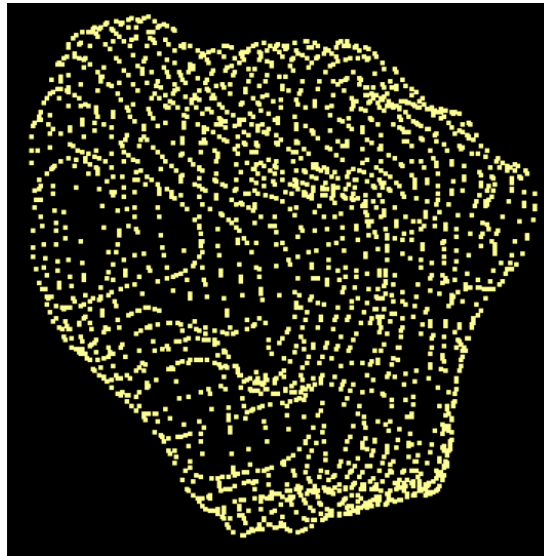


**Figure 3.3.** Three-Dimensional Plot of Radius Contours in PED

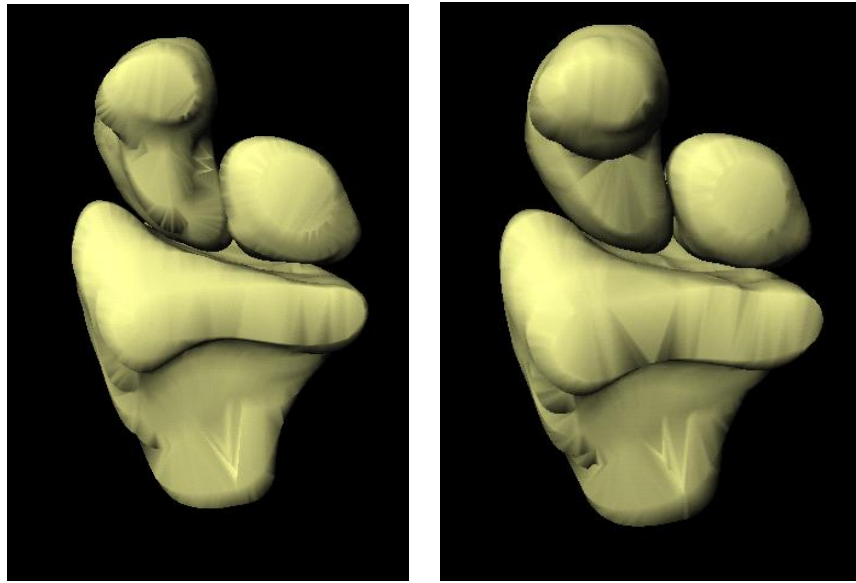
For the segmented cartilage models, the bones with cartilage were directly segmented from the relaxed scan images. The bones were also segmented without cartilage from the relaxed image sets for the projected cartilage models. Once the bone only models were generated, a Matlab program was used to project a 1 mm expansion normal to the entire bone surface, to simulate a uniform, ideal cartilage surface.

The position and orientation of the carpal bones in the relaxed and grasp positions is different. To study the joint contact mechanics, it was necessary to find the kinematic transformation for each bone from the unloaded to the loaded configuration. These transformations were determined by a series of 3D voxel image registrations (Analyze 5.0, Analyze Direct, Lenexa, KS). Bone volumes for each individual bone were isolated from both the loaded and unloaded image sets. The

radius was chosen as a fixed reference. The kinematic translation of the radius from loaded to unloaded is then applied to the loaded volumes of the scaphoid and lunate. The unloaded scaphoid and lunate are then registered to the transformed scaphoid and lunate to obtain their final kinematics, respectively. These kinematics are represented as an attitude and translation vector for input into the Joint\_Model program.<sup>25</sup> The Joint\_Model program produced data for contact area, contact force, and peak contact pressure. It was then possible to compare directly the data from each method of cartilage modeling side by side and to the Tekscan sensor data.

### **3.3. Results**

The geometries of the projected and segmented cartilage models were similar and qualitatively appeared to be accurate (Fig. 3.4). The projected models appeared slightly larger than the segmented models. However, calculation of bone volumes showed that there was not consistent overestimation or underestimation of bone volume in the projected models (Table 3.1, Fig. 3.5)



(a)

(b)

**Figure 3.4.** Manually generated bone models for specimen 2.  
 (a) Segmented cartilage (b) Projected cartilage

**Table 3.1.** Volume of Segmented and Projected Lunate and Scaphoid Bones.

	Projected Volume (mm <sup>3</sup> )	Segmented Volume (mm <sup>3</sup> )	Projected as % of Cartilage Models
S1 Lunate	2876	1969	146.06%
S1 Scaphoid	3476	1382	251.52%
S2 Lunate	1521	1257	121.00%
S2 Scaphoid	2453	2804	87.48%
S3 Lunate	4308	4890	88.10%
S3 Scaphoid	8144	8349	97.54%

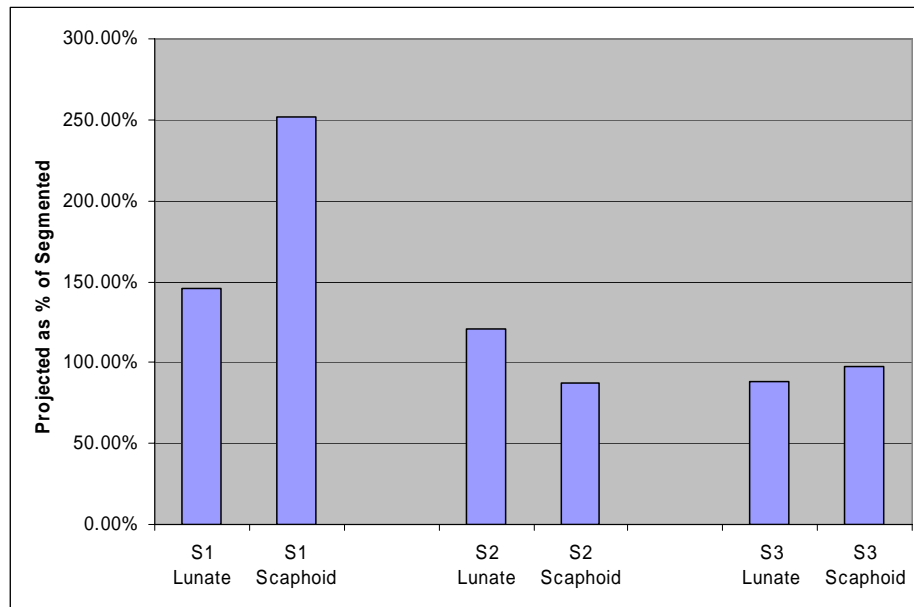


**Figure 3.5** Projected model volume as a percent of segmented model volume.

The Joint\_Model program produced results that were visually and quantitatively assessed (Fig. 3.4, Table 3.2). It was visually apparent that the projected models produced different contact pressure distributions than the segmented models, as evidenced by the larger contact areas (Fig. 3.6). The average radioscaphoid (RS) and radiolunate (RL) contact areas for the projected models were 71.2 and 67.6 mm<sup>2</sup>, respectively. This is compared to average contact areas of 39.9 and 10.73 mm<sup>2</sup> reported by the Tekscan sensor and 52.30 and 47.7 mm<sup>2</sup> measured by the segmented model. Projected model articulations exhibited higher peak pressures, with an average RS pressure of 3.57 MPa and an average RL pressure of 2.8 MPa. In comparison, Tekscan and segmented model results were closer to one another, with Tekscan reporting an average RS pressure of 1.2 MPa and the segmented models showing an

average RS pressure of 1.53 MPa. The combination of projected model contact areas and pressures also resulted in higher RS and RL contact forces (avg. 135.1 N and avg. 69.1 N) compared to the segmented models (avg. 35.4 N and avg. 32.43 N). Because of this combination of higher pressure and contact area, the projected models predicted contact forces on average 710% higher than the average force reported by the Tekscan sensor. In comparison, the segmented models were only an average of 213% higher than the Tekscan sensor in this experiment. Although neither modeling approach precisely matched all the Tekscan data, the projected data showed substantially larger differences than the segmented data (Table 3.2).

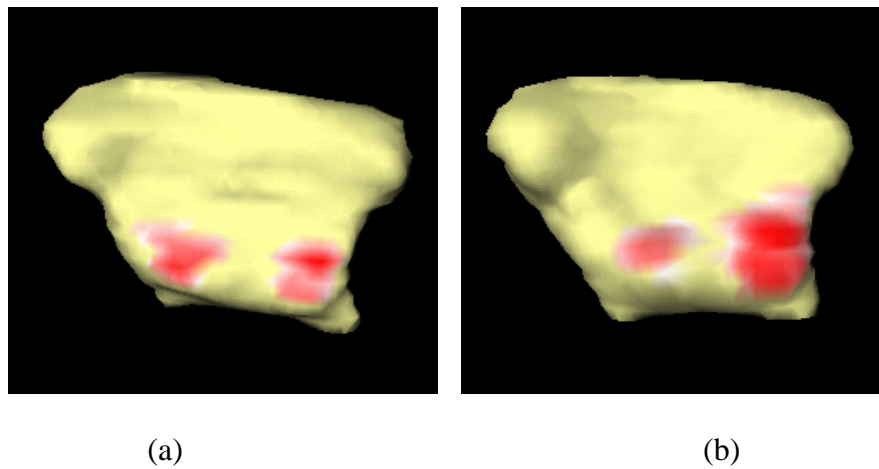


**Figure 3.6.** Sample pressure distributions for specimen 1. Shown here are is the articular surface of the radius. (a) segmented cartilage (b) projected cartilage

**Table 3.2.** Pressure, force, and contact area as calculated by each of the three methods. Radioscaphoid and Radiolunate joints shown here. Although the Joint\_Model program reported scapholunar data, because it could not be confirmed with the Tekscan sensor, it was omitted from this manuscript.

Joint	Method	Specimen 1			Specimen 2			Specimen 3		
		Peak Press. (Mpa)	Force (N)	Area (mm)	Peak Press. (Mpa)	Force (N)	Area (mm)	Peak Press. (Mpa)	Force (N)	Area (mm)
R-S	Tekscan	1.5	44.8	61.7	1.2	7.0	18.1	0.9	15.5	39.9
	Segmented	1.9	36.2	42.2	1.8	48.0	48.3	0.9	22	66.4
	Projected	4.4	198.5	88.0	2.4	72.1	58.2	3.9	134.8	67.5
R-L	Tekscan	0.7	9.8	18.1	0.4	1.9	7.3	0.4	6.8	6.8
	Segmented	2.1	28.4	32.1	1.5	35.4	50.4	1.6	33.5	60.8
	Projected	3.2	55.4	40.2	2.8	60.8	51.6	2.4	91.0	111

### 3.4. Discussion

Though the geometry of projected cartilage models appeared to be anatomical, overestimation of joint forces occurred. Furthermore, the magnitude of error for each articulation in the projected models was not consistent from specimen to specimen, making it difficult to draw a conclusion about the effect of projected cartilage modeling on a particular articulation. Since the contact areas are similar, projected models appear to overestimate penetration depth and pressure, due to a lack of “tapering” of cartilage thickness (resulting in geometric errors).

Although the segmented cartilage models showed differences from the Tekscan data, the results were consistently closer than the projected cartilage results. It is important to note that there is also error attributed to the experimental technique and the accuracy of the Tekscan sensor. Our studies indicate that the Tekscan sensor

produces about 80% of measurements within 11% of actual values of forces in such experiments.

The results of this study indicate that whenever possible, the cartilage surface in a joint should be segmented from an MR image set. When it is necessary to use projected cartilage models the investigators should be aware of possible errors. The most appropriate models with projected cartilage will be comparative studies that only consider relative changes between models, and not absolute values. The applied loading and/or kinematics, combined with the complex geometry of the bone makes these models extremely sensitive to cartilage surface geometry. Although CT may yield more accurate models of bone (only), the MR data allows accurate modeling of both the bone and the cartilage surface.

The results of this study apply not only to surface modeling of joints, but also to discrete-element models (rigid-body spring models) and finite element models. The results also have implications for distance-based contact area estimates calculated from bone proximity. All investigators using projected cartilage models should carefully consider their limitations.

### 3.5 References

1. Ahn HS, DiAngelo DJ. Biomechanical testing simulation of a cadaver spine specimen: development and evaluation study. *Spine* 2007;32(11):E330-6.
2. Anderson AE, Peters CL, Tuttle BD, Weiss JA. Subject-specific finite element model of the pelvis: development, validation and sensitivity studies. *J Biomech Eng* 2005;127(3):364-73.
3. Anderson DD, Daniel TE. A contact-coupled finite element analysis of the radiocarpal joint. *Semin Arthroplasty* 1995;6(1):30-6.
4. Anderson DD, Deshpande BR, Daniel TE, Baratz ME. A three-dimensional finite element model of the radiocarpal joint: distal radius fracture step-off and stress transfer. *Iowa Orthop J* 2005;25:108-17.
5. Anderson DD, Goldsworthy JK, Li W, James Rudert M, Tochigi Y, Brown TD. Physical validation of a patient-specific contact finite element model of the ankle. *J Biomech* 2007;40(8):1662-9.
6. Beek M, Koolstra JH, van Ruijven LJ, van Eijden TM. Three-dimensional finite element analysis of the cartilaginous structures in the human temporomandibular joint. *J Dent Res* 2001;80(10):1913-8.
7. Buchler P, Ramaniraka NA, Rakotomanana LR, Iannotti JP, Farron A. A finite element model of the shoulder: application to the comparison of normal and osteoarthritic joints. *Clin Biomech (Bristol, Avon)* 2002;17(9-10):630-9.

8. Carrigan SD, Whiteside RA, Pichora DR, Small CF. Development of a three-dimensional finite element model for carpal load transmission in a static neutral posture. *Ann Biomed Eng* 2003;31(6):718-25.
9. Donahue TL, Hull ML, Rashid MM, Jacobs CR. A finite element model of the human knee joint for the study of tibio-femoral contact. *J Biomech Eng* 2002;124(3):273-80.
10. Fregly BJ, Bei Y, Sylvester ME. Experimental evaluation of an elastic foundation model to predict contact pressures in knee replacements. *J Biomech* 2003;36(11):1659-68.
11. Fregly BJ, Sawyer WG, Harman MK, Banks SA. Computational wear prediction of a total knee replacement from in vivo kinematics. *J Biomech* 2005;38(2):305-14.
12. Gardiner JC, Weiss JA. Subject-specific finite element analysis of the human medial collateral ligament during valgus knee loading. *J Orthop Res* 2003;21(6):1098-106.
13. Genda E, Horii E. Theoretical stress analysis in wrist joint--neutral position and functional position. *J Hand Surg [Br]* 2000;25(3):292-5.
14. Genda E, Konishi N, Hasegawa Y, Miura T. A computer simulation study of normal and abnormal hip joint contact pressure. *Arch Orthop Trauma Surg* 1995;114(4):202-6.
15. Koolstra JH, van Eijden TM. Combined finite-element and rigid-body analysis of human jaw joint dynamics. *J Biomech* 2005;38(12):2431-9.

16. Kwak SD, Blankevoort L, Ateshian GA. A Mathematical Formulation for 3D Quasi-Static Multibody Models of Diarthrodial Joints. *Comput Methods Biomech Biomed Engin* 2000;3(1):41-64.
17. Li G, Gil J, Kanamori A, Woo SL. A validated three-dimensional computational model of a human knee joint. *J Biomech Eng* 1999;121(6):657-62.
18. Li Z, Alonso JE, Kim JE, Davidson JS, Etheridge BS, Eberhardt AW. Three-dimensional finite element models of the human pubic symphysis with viscohyperelastic soft tissues. *Ann Biomed Eng* 2006;34(9):1452-62.
19. Manal K, Lu X, Nieuwenhuis MK, Helders PJ, Buchanan TS. Force transmission through the juvenile idiopathic arthritic wrist: a novel approach using a sliding rigid body spring model. *J Biomech* 2002;35(1):125-33.
20. Mesfar W, Shirazi-Adl A. Biomechanics of the knee joint in flexion under various quadriceps forces. *Knee* 2005;12(6):424-34.
21. Penrose JM, Holt GM, Beaugonin M, Hose DR. Development of an accurate three-dimensional finite element knee model. *Comput Methods Biomech Biomed Engin* 2002;5(4):291-300.
22. Pillai RR, Thoomukuntla B, Ateshian GA, Fischer KJ. MRI-based modeling for evaluation of in vivo contact mechanics in the human wrist during active light grasp. *J Biomech* 2007.
23. Taddei F, Pancanti A, Viceconti M. An improved method for the automatic mapping of computed tomography numbers onto finite element models. *Med Eng Phys* 2004;26(1):61-9.

24. Tsumura H, Miura H, Iwamoto Y. Three-dimensional pressure distribution of the human hip joint--comparison between normal hips and dysplastic hips. *Fukuoka Igaku Zasshi* 1998;89(4):109-18.
25. Ueki K, Nakagawa K, Takatsuka S, Yamamoto E. The change of stress distribution on the condyle after mandibular setback surgery. *Eur J Orthod* 2006;28(5):433-9.
26. Woltring HJ. 3-D attitude representation of human joints: a standardization proposal. *J Biomech* 1994;27(12):1399-414.

## **Chapter 4. Validation of MRI-Based Modeling for Joint Contact Mechanics**

### **Abstract**

The purpose of this study was to determine the validity of an MRI-based modeling technique for use in joint contact mechanics. Five cadaver forearms were given a volar dissection of the wrist, to allow insertion of either Pressurex film or a Tekscan sensor. The forearm was dissected, and five tendons, the flexor digitorum profundus (FDP), flexor digitorum superficialis (FDS), flexor pollicis longus (FPL), extensor carpi ulnaris (ECU), and extensor carpi radialis (ECR) were isolated as a method of applying loads to simulate grasp of the hand. The wrist was also imaged (in unloaded and loaded states) in an MRI scanner and 3D models of the radius, lunate, and scaphoid bones and their cartilage were created. The kinematic transformations of these bones from unloaded to loaded configuration were found using normalized mutual information registration. The kinematics were applied to the bone models, and analysis was done to determine the contact area, contact force, and peak pressure in the radioscaphoid, radiolunate, and scapholunate joints. These data were compared to the experimental Tekscan and Pressurex data. Contact area between bones was also directly measured from the loaded MR image sets. It was found that the MRI-based model had a significant agreement in contact area with the direct contact area measurement. The Tekscan and MRI-based model technique showed similar measures of contact force, and the Pressurex and MRI-based technique showed similar measures of peak pressure. It is therefore believed that the

MRI-based modeling technique is a feasible method of analyzing joint contact mechanics.

#### **4.1. Introduction**

With an aging U.S. population, the need for cost-effective tools for the detection and prevention of arthritis is increasing. The development of these tools has been an important area of investigation for both clinicians and biomechanical engineers.

One area of development in joint contact analysis is computational modeling. If effective models that simulate *in vivo* conditions can be developed, it will pave the way for new diagnoses and preventative measures against arthritis.

Several computational methods have been developed to model joint mechanics. Finite element method (FEM) has gained popularity as increasing computational speed has allowed more complex models to be created and analyzed.<sup>1, 3, 7, 14, 20, 21, 23, 24, 26</sup> These models generally have highly accurate geometry of bones from CT or MRI data. If the model is being developed from CT and is to be used to study contact forces and mechanics and not just kinematics, a cartilage mesh layer is often projected from the bone surface, at a uniform height determined by the researcher.<sup>2, 4, 5, 6, 8, 9, 18</sup> Models developed from MRI generally obtain bone and cartilage geometry from the images. Accuracy of these models is determined by the accuracy of the geometry, material properties, mesh quality, and boundary conditions.

Another method of joint analysis is rigid body spring modeling (RBSM). Like models created for FEM analysis, these models create accurate depictions of bones.

However, unlike the volume meshes for cartilage in FEM, rigid body spring models simulate articular surfaces as finite sets of compression springs.<sup>12, 13, 15, 16, 22, 28, 30</sup>

Cartilage is simulated on one or both bones in contact, and the spring properties are defined based on the bulk properties of the cartilage joint of interest. Tendons and ligaments are modeled as tensile springs if whole joint mechanics are being analyzed. These RBSM models benefit from ease of development and computational efficiency compared to FEM models.

A third method is multi-body contact modeling. Often, the joint of interest is modeled as quasi-static, in that the boundary conditions are defined as fixed for a given configuration at a specific point in time. Bone models are created from the relaxed joint, so that when the kinematics of interest are applied, interpenetration of the bone models occurs. Contact mechanics are calculated based on this penetration depth of the bones in contact.<sup>19, 25</sup> There exist several multi-body software programs which focus on this technique (ADAMS, DADS, Working Model, DYNAMAN, Articulated Total Body Model, etc.). Surface contact models maintain the computational efficiency of RBSM, but have continuous surfaces and more robust and flexible contact rules. Two studies in particular both elucidate this method as well as provide justification for this work.<sup>25, 27</sup>

Pillai et al. developed a method to determine the radiocarpal joint contact mechanics from MRI-based models.<sup>25</sup> MR images of the wrist of four human subjects were acquired in both grasp and relaxed states, using a 1.5 Tesla whole body MRI scanner with a flexible wrist coil. The image sets had an in-plane resolution of 0.3125

mm and a slice thickness of 2 mm. Three-dimensional models of the radius, scaphoid, and lunate bones (with cartilage) were created from the relaxed image sets. Kinematic transformations from the unloaded to the loaded configuration were applied to the models. These kinematics were obtained by surface registration of bone only models of the relaxed and grasp image sets. The joint contact mechanics were investigated using the Joint\_Model program developed at Columbia University.<sup>19</sup> The contact pressure distribution, contact forces, and contact areas were analyzed for each of the articulations of the radiocarpal joint (radioscaphoid, radiolunate, and scapholunate). The results of that study were promising, although preliminary, and encouraged further investigation. However, that study had several limitations. The image resolution and signal-to-noise ratio were lower than desired, the slice thickness was 2 mm, the surface registration technique lacked precision, and the overall technique had not been validated.

Considering these limitations, an initial validation study was conducted by Thoomukuntla et al., which addressed many of the limitations of Pillai's work.<sup>27</sup> This study increased image resolution and the signal-to-noise ratio using a higher field (9.4 Tesla) MR image system. A gradient recall echo sequence was used and an in-plane resolution of 0.12 mm with a slice thickness of 1 mm was obtained. As with Pillai's work, 3D models of the radius, scaphoid and lunate bones including articular cartilage were produced from the relaxed image sets. In this case, however, grasp and relaxed image sets were taken of 3 cadaveric forearm specimens, which allowed dissection of the forearm and radiocarpal joint. The dissection of the radiocarpal joint allowed the

insertion of either a Pressurex pressure sensitive film or a Tekscan piezoresistive sensor into the joint space. Light grasp was simulated by static weights which applied tension (via an apparatus) to the flexor digitorum profundus (FDP), flexor digitorum superficialis (FDS), and flexor pollicis longus (FPS) tendons. The forearm bones (radius and ulna) were fixed to the loading apparatus in neutral rotation of the forearm.

Another refinement in this work was the use of volume based registration for obtaining transformation kinematics. Isolated bone images were created from both the relaxed and grasp MR image sets. Images sets were then compiled into a volume using Analyze 5.0 (Analyze Direct, Inc. Lenexa, KS). The normalized mutual information method was used to determine the transformation of the lunate and scaphoid bones from the relaxed to grasp states. These kinematic descriptions were implemented with the bone (and cartilage) models in the Joint\_Model program to determine contact mechanics.

Results were encouraging. Peak pressures were within expected values, and interpenetration depth of the models did not exceed realistic values. Furthermore, there was a qualitative match between the intensity and location of contact from experimental measures and the models.

One method used in this study was direct calculation of contact area from the MR image sets. Because of the higher resolution and thinner slice thickness, it was possible to accurately calculate the contact area from each grasp image set. These contact area values closely matched the contact areas found from the models.

The purpose of this work is to continue validation of this novel method by testing a further five specimens, as well as to continue refinement of the experimental technique. After validation and further research, this method may develop into clinical tools to diagnose and treat arthritis.

## **4.2. Methods**

### **4.2.1 Specimen Preparation**

For this experiment, 5 human cadaveric forearms were used. The dissection process had two major steps. First the required tendons and bones were exposed and isolated. Later a volar dissection of the radiocarpal joint capsule was performed.

In the work done by Thoomukuntla, only the FDS, FDP and FPL tendons were used. When loading the wrist through these three tendons, it became necessary to secure the hand to the apparatus; the loads caused the wrist to flex, as well as flexing the fingers. For the specimens listed here, a new technique was used. Along with the three flexor tendons, two extensor tendons, the extensor carpi ulnaris (ECU) and extensor carpi radialis (ECR) were also isolated (Fig. 4.1). The extensor carpi radialis longus and extensor carpi radialis brevis were sewn together and considered “one tendon” for this experiment. All five tendons were tied with a suture loop, so that they could be axially loaded. The suture loops were secured to loops of 40 lb. (178 N) test fishing line, and connected through a pulley system to the water jugs which provided

static load. By loading the extensors along with the flexor tendons, a more realistic simulation of light grasp was performed.

All remaining soft tissue along a ten centimeter section of the radius and ulna was removed (although the interosseous membrane was left intact). Two 6.35 mm holes were drilled through the radius, and one through the ulna, and were used to attach the specimen to a plate (Fig. 4.1). Care was taken to align the holes so the forearm was in neutral rotation, and to ensure it would remain so during experimental testing and MR imaging.

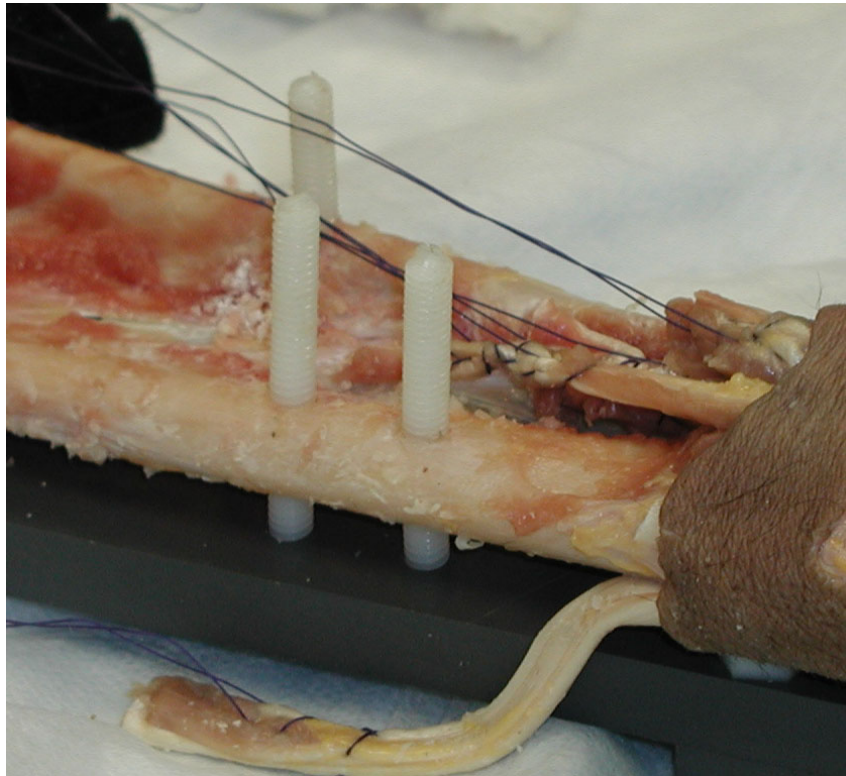


**Figure 4.1** Isolation and fixation of radius and ulna to PVC plate. Isolated and sutured tendons also shown.

#### **4.2.2 Experimental Setup**

All materials used in the experimental setup were made of plastic so as to be non-ferrous, and compatible with the MRI scanner. The setup consisted of a stand, a pulley plate, and four extension plates three inches (75 mm) wide, 0.5 inches (12.5 mm) thick, and of varying lengths (Fig. 4.2, 4.3). The extension plates were used to connect the specimen plate to the pulley plate and weight stand. Thus, the whole setup was stable and capable of applying consistent loads, and the wrist could be placed at the isocenter of the MRI scanner. Weights were plastic jugs filled with a measured amount of water. For this experiment a total of 110N was applied, the ECU and ECR were loaded with 30 N each, the FDS and FDP were loaded with 20 N each, and the FPL was loaded with 10 N. These loads, chosen because they are proportionally similar to the cross-sectional area of the muscles they simulate, were applied during experimental work as well as during MRI scanning. Also, during the application of loads, a 1.5 inch (38.1 mm) outside diameter cylindrical PVC pipe section was placed in the fingers of the specimen as an object to grasp.



**Figure 4.2** Partial experimental Setup. Shown here are the five water jugs used as weights to simulate light grasp through the tendons of the wrist.

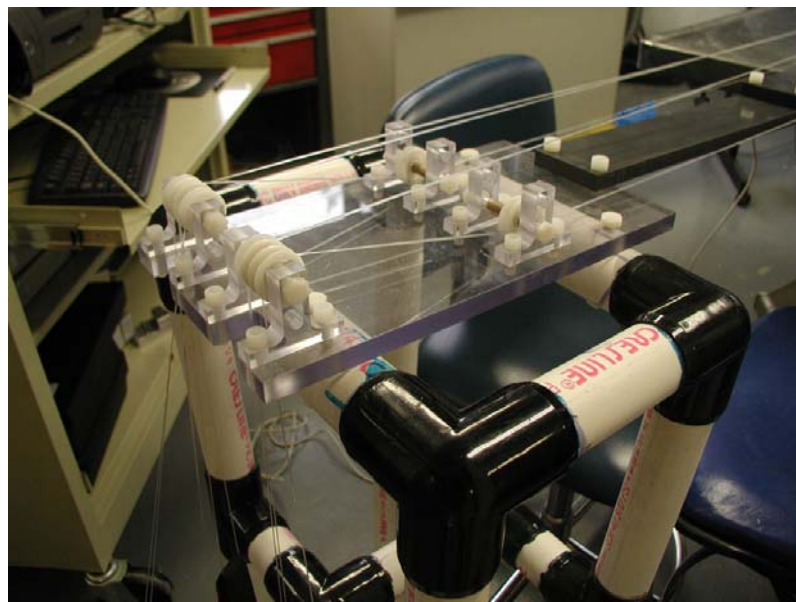


**Figure 4.3** Experimental Setup. Shown here is the pulley assembly used to direct the loads from the water jugs through the three flexor and two extensor tendons. Extensor tendon lines ran under a low pulley before going over the high pulleys to the left.

### 4.2.3 Experimental Validation

Several methods exist to measure contact pressures and forces in human joints. These include piezoelectric films, strain gauges, Fuji film, and piezoresistive sensors. For this study, pressure sensitive film (Pressurex Films, Sensor Products Corp., East Hanover, N.J.) and a piezoresistive sensor (Tekscan Model #4201, Tekscan Inc., South Boston, MA) were chosen.

#### 4.2.3.1 Pressurex Film

Pressurex<sup>®</sup> film (Sensor Products Inc., East Hanover, NJ) reveals the pressure distribution that occurs between any two surfaces when the film is placed between them. The film contains microcapsules of ink that burst at different pressures. A developer reveals and locks the image on the film (Fig. 4.4). The color intensity (up to saturation) is proportional to the amount of pressure applied to it. The higher the pressure, the more intense the color.

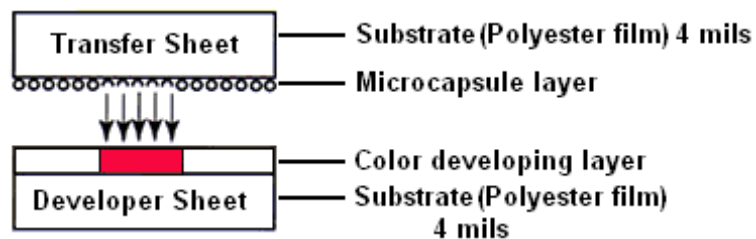


**Figure 4.4** Cross Section of Pressurex Film (Sensor Products Inc., East Hanover, NJ)

Pressurex is a super thin (4-8 mils, 1 mil= 0.0254 mm = 0.001 in) film similar to a sheet of standard copy paper. This facilitates its use on curved surfaces, and it is ideal for invasive environments and tight spaces. Pressure can be determined by comparison with a color calibration chart provided with the film, or by calibration and interpretation using image analysis with software (such as Adobe Photoshop). Calibration and interpretation is discussed in detail in Chapter 2 and later in this chapter. For this study it was decided to use “Super Low” Pressurex Film with a pressure range of 70-350 PSI (0.48-2.41 MPa). Physical specifications can be found in Table 4.1.

**Table 4.1** Physical Specifications of the Pressurex Film

Temperature Range	41° - 95°F (5° - 35° C) (Higher for brief exposure)
Humidity Range	20 - 90% RH Gauge 4 - 8 mils (100 to 200 microns)
Spatial Resolution	5 to 15 microns Substrate Polyethylene Terephthalate (PET)
Accuracy	±10% visual ±1% utilizing optical measurement system
Shelf Life	2 Years

Calibration of the film was performed under controlled conditions. A cylindrical (0.625 in OD), flat indenter and flat block were lined with a layer of shore 80A rubber. This rubber had a thickness of 1.6 mm and a modulus of elasticity similar to human articular cartilage. The film was placed between the surfaces of the rubber on the flat block and indenter. Loads of 100 N to 1000N were applied in increments of 100 N. Each load was applied for 30 seconds, then released. The film was subsequently scanned at 72 dpi into image files which could be analyzed by Adobe Photoshop.

A circular selection tool identical in size to the indenter (0.625 in diameter) was used to select each area. Average red, green, and blue intensity values were then recorded. The calibration curve was based on normalized red values minus normalized blue. The normalized red values were obtained by dividing the red intensity value by the sum of the red, green, and blue intensity values. Similarly, the normalized blue values were obtained by dividing the blue intensity by the sum of the red, blue and green values. The normalized red minus normalized blue value was then compared to the applied pressure to develop a cubic calibration curve (Fig. 4.5) which could be used to calculate contact pressures during specimen testing. Each calibration was done immediately before testing of the specimen, to limit environmental effects on film performance.

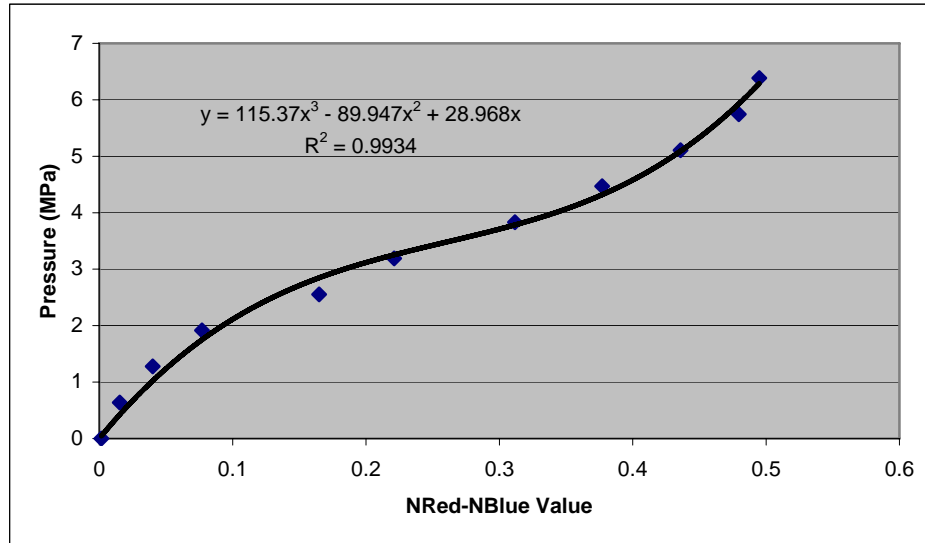


**Figure 4.5** Sample calibration curve (Specimen 3) showing cubic regression equation and correlation coefficient.

To test specimens, a basic template was created to match the two fossa on the radius. This was also to minimize crimping and other artifacts on the film. A small volar tab was added to the film, to help with insertion and removal, as well clarify the dorsal and volar edges. The film and developer sheets were wrapped in a thin layer of plastic wrap, to prevent saline solution and synovial fluid from altering film performance.

The film was then inserted into the radiocarpal joint and the tendon loads were applied. Specifically, the ECU and ECR loads were first applied, then the FDS FDP, and finally the FPL loads were applied. This order was repeated for all experiments and specimens. The load was held for approximately 30 seconds then released, and the film was carefully removed. This procedure was repeated five times per specimen.

#### **4.2.3.2 Tekscan Sensor**

Tekscan pressure measurement devices (Tekscan Inc., South Boston, MA) are “thin film” electronic sensors that provide reliable and accurate force and pressure data. The analysis of dynamic pressure distribution is made possible by the real-time feedback of Tekscan’s sensing system. Tekscan pressure sensors provide lower spatial resolution than Pressurex film, but the ability to capture data in real-time removes sensitivity to insertion and removal artifacts.

The Tekscan system used for joint analysis was the K-Scan<sup>TM</sup> System. This system is comprised of controlling electronics, sensor, and Windows-compatible

software. The sensor chosen (Fig. 4.6 and Table 4.2) was the Wrist Sensor, Model #4201 (Tekscan Inc., South Boston, MA).



**Figure 4.6** Wrist Sensor, Model #4201.

**Table 4.2** Wrist Sensor, Model #4201 Specifications

No. of Sensels	264
Spatial Resolution	3.629 mm <sup>2</sup>
Size of Entire Sensor	50 mm X 430 mm (including electronic connection pad)
Technology	Resistive
Calibration	Application of controlled/known force
Sampling Rate	127 Hz
Dynamic Range	34 min kPa (5 PSI) - 13.8 max MPa (2000 PSI)
Grid Size	24 X 11 sensels (46 X 21 mm)

Calibration of the Tekscan followed similar methods as with the Pressurex Film. Prior to calibration of the sensor, it was trimmed approximately 2 mm on each side, and resealed. This allowed it to better fit into the radiocarpal joint, without compromising sensor integrity. The Tekscan sensor was placed between two plates, each with a 13 mm X 13 mm piece of shore 80A rubber on it. The plates were then pressed together with a known force using an Instron Materials Testing Machine

(Model #8511, Instron Corp., Canton, MA) at increments of 100 N from 100 N to 1000 N. Raw values were then output from each sensel. Because the area of contact was known, it was possible to create a quadratic regression curve relating the pressure applied to the average raw value of all active sensels (Fig. 4.7). This curve was created for each specimen, immediately before specimen testing.

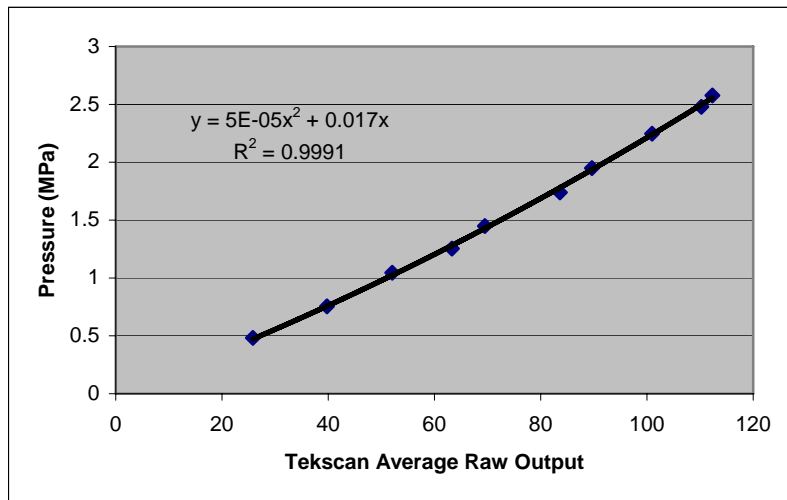


**Figure 4.7** Sample calibration curve (Specimen 2) for Tekscan sensor, showing quadratic regression equation and correlation coefficient.

The experimental setup for the Tekscan sensor was identical to that used for the Pressurex film. The Tekscan sensor grid was placed in the radiocarpal joints. The extensor and flexor tendons were loaded in the order stated previously. As soon as all tendons were loaded and stable, pressure data from the sensor was acquired and saved. This data was later processed using the Tekscan calibration.

#### 4.2.4 Specimen Imaging and Modeling

MR images for this study were acquired using a 9.4 Tesla research scanner (Unity INOVA Animal Systems, Varian Inc., Palo Alto, CA) using a gradient recall echo sequence – TR 800 ms, TE 7.81 ms (minimum), flip 45°, NEX (averages) = 4. Scans were performed in the frontal plane with a slice thickness of 1 mm. Field of view was 70 mm X 140 mm a resolution of 512 X 1024 pixels for specimens 1, 2, and 5, giving a resolution of 0.136 mm. The field of view for specimen 3 was 60 mm X 60 mm with a resolution of 512 X 512 pixels, giving a resolution of 0.117 mm. The field of view for specimen 4 was 120 mm X 60 mm, with a resolution of 512 X 1024 pixels. Specimen 4 had a resolution of 0.117 mm. Slice number varied from 28 – 30 slices per scan. For each specimen, two image sets were obtained – loaded and unloaded. Unloaded specifically refers to no loading of the flexor or extensor tendons, and loaded refers to when all five tendons were loaded as described previously.

Once images were obtained, segmentation of unloaded scans was performed for the scaphoid, lunate, and radius bones, including cartilage. Segmentation was performed manually in MPXImage (Ted Manson, 1998, University of Pittsburgh) by creating a series of B-spline curves around each bone and its cartilage in a single image. The 2D curves were compiled into a 3D point cloud. This made it possible to develop all three bone models in the same local (image) coordinate system.

Point clouds were then converted into surface models using Geomagic Studio 9 (Raindrop Geomagic, Research Triangle Park, NC). The surface models were then imported into the Joint\_Model program.

To obtain transformation kinematics of the bones from the unloaded to the loaded position, 3D image registration was performed. To register individual bones, it was necessary to isolate the images of each bone (without cartilage) from the image set (Fig. 4.8).

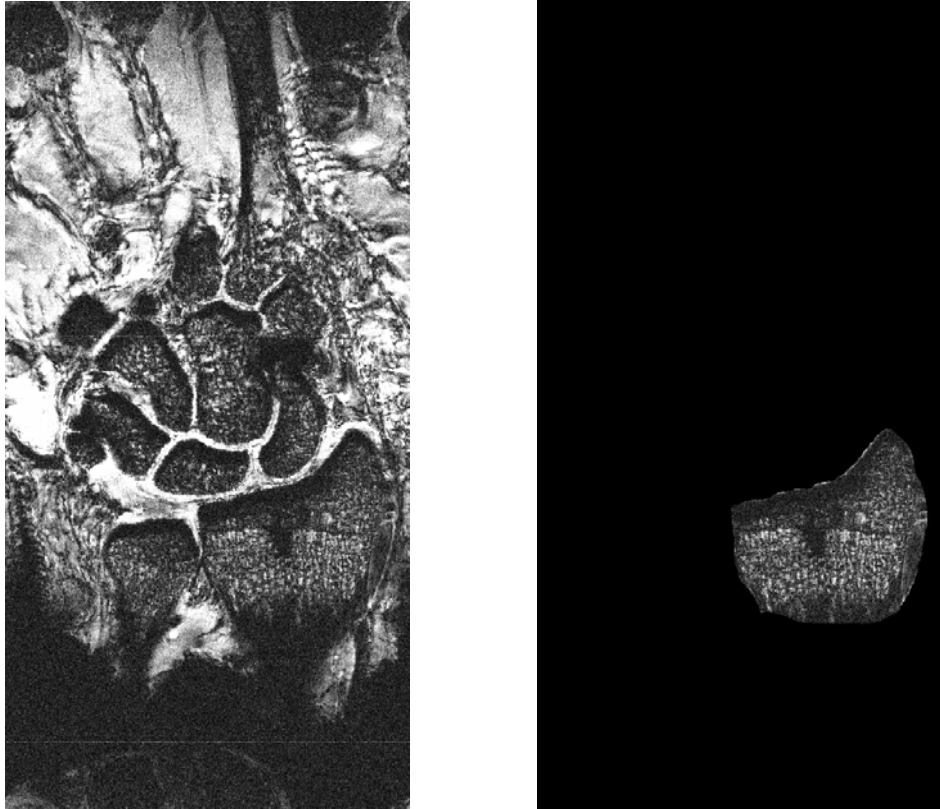


**Figure 4.8** MR Image (left) and isolated radius bone (right) for use in kinematic registration.

These isolated bone images could then be compiled into a volume using Analyze 5.0 (AnalyzeDirect, Lenexa, KS). Using Analyze, 3D voxel-based registration was performed between two image volumes. A “Voxel Match” algorithm based on Normalized Mutual Information (NMI) was used to register the image volumes accurately and quickly.

To obtain kinematic descriptions, first the radius was chosen as the “fixed” reference bone (no rotation or translation). Next, the transformation to align the loaded image set with the unloaded image set was found by registering the loaded radius volume (match) to the isolated unloaded radius volume (base). The Analyze software then calculated a 4X4 transformation matrix. This transformation was then applied to the isolated loaded scaphoid and lunate bones *before* they were registered, effectively placing them in the unloaded image coordinate system. The isolated, unloaded scaphoid and lunate bone volumes were then registered to their respective transformed isolated loaded bones. The resulting 4X4 transformation matrices constituted appropriate kinematics to move the surface models from the unloaded image set into the loaded configuration, but in the left-hand Analyze coordinate system.

The input for the Joint\_Model program contains both the surface models and the kinematic transformation for each of the individual bones. However, the format for the kinematic description of each bone is in the form of attitude and translation vectors, so a standard conversion was made from the 3X3 DCM portion of the Analyze transformation matrix to the attitude vector.<sup>30</sup> The translation vector was also obtained from the 4X4 Analyze matrix. The kinematics were also corrected for the left-handed Analyze coordinate system.

#### 4.2.5 Execution of Model Simulation

The Joint\_Model program [Kwak et al., Columbia University, 2000] serves as an effective modeling tool for this work because of several key features. Bones, cartilage, ligaments and tendons can all be modeled individually. The program allows wrapping of soft tissues around bone, and it allows 3D articular contact between bodies. Maximum penetration depth is calculated for each pair of contacting bodies, as are pressures at each vertex for each contact pair. This pressure distribution can be displayed as a saturation map and the peak pressure value at the contact is provided. The program also calculates contact force and contact area for each articulation. Finally, the program is computationally efficient (compared to FEM).

The input for the Joint\_Model program is a text file containing information about the bodies to be modeled and the nature of the contact between each pair of bodies. The CTPSTRL contact rule was used, which models the contact pressure as linearly proportional to strain. This contact rule requires material properties of the contact surfaces (elastic modulus) and the total thickness of the cartilage on both bodies being modeled. A modulus of 4 MPa and a cartilage thickness of 1 mm on each bone (2 mm total) were used.<sup>19</sup> The main Joint\_Model input file refers to the surface geometry files for each body. In addition, contact pairs must be specified. Kinematics for each body was applied by directly specifying them in the input file. For this analysis, body motion was set as fixed (displacement driven) and mechanical descriptions were based entirely on the resulting penetration depth. Once the carpal bone kinematics

were applied and the solution was determined, the program provided contact area, contact force, and peak contact pressure for each contact pair.

#### **4.2.6 Direct Contact Area Measurement from MR Images**

Contact area measurements were also obtained directly from the MR images. These measurements served as a process of verification of model contact area only. The method used was straightforward, and can be used in human subjects to help verify modeling accuracy. To calculate surface area, segmentation was done of only the contact region between the two bones being studied, for example between the radius and scaphoid. Using the grasp (loaded) image set, an arc was created along the contact surface of the two bones and points along this arc were written to a text file (Fig. 4.9). The text file was then imported into a Microsoft Excel workbook in which all the text files were compiled for each pair of bones. The arc lengths between adjacent points were calculated. This was then summed and calculation of contact area was performed (by multiplying the arc lengths by the slice thickness of 1 mm).

The text file contains data in the form of X and Y coordinates. For these contacts, dX and dY are calculated where

$$dX = X_{i+1} - X_i \quad 4.2-1$$

$$dY = Y_{i+1} - Y_i \quad 4.2-2$$

The resulting dX and dY values were squared, summed and the square root was taken to get the distance between consecutive 2D points.

$$dL = \sqrt{dX^2 + dY^2} \quad 4.2-3$$

The sum of these lengths  $dL$  yielded the total arc length for a single contact on a single image. Multiplication of that length by the slice thickness yielded an area for each slice. By summing all the contact areas for all the slices the total contact area was measured.

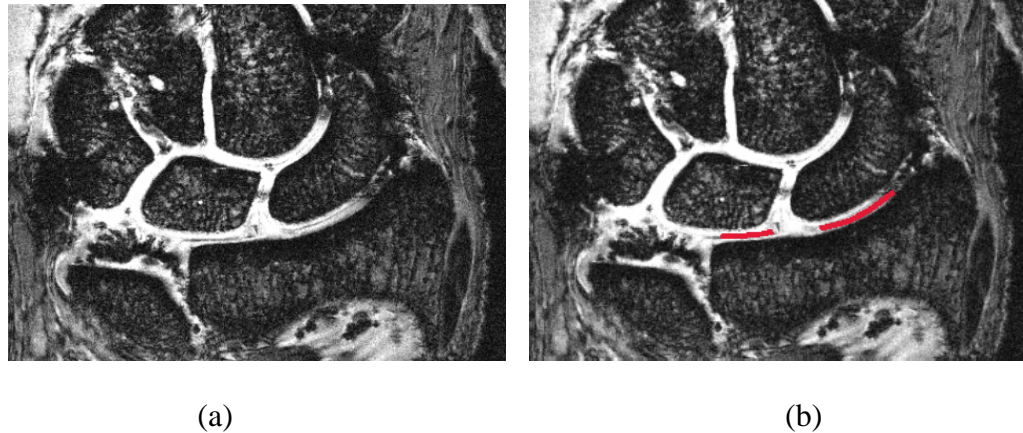


**Figure. 4.9** Radius, lunate, and scaphoid bones, the contact area is visible (a), and then isolated (b) for segmentation.

#### 4.2.7 Statistical Analysis

Once data for contact force, contact area, and peak pressure were collected from the Tekscan sensor, Pressurex film, and the MRI-based model, they were compared qualitatively and quantitatively. Regression analysis was performed on each measurement method for force, area, or pressure, to see if there was a significant correlation between any experimental measure and the MRI-based model data. Correlation coefficients and significance values were calculated comparing the Tekscan sensor forces with those from the MRI-based model as well as comparing the Pressurex film forces and the MRI-based model. The same two comparisons were

made for the peak pressure results, comparing Tekscan to MRI-based model data, and comparing Pressurex to the MRI-based model data. Lastly, the contact areas were compared. Correlation coefficients and significance values were found comparing the MRI-based models to each the Tekscan sensor, Pressurex film, and the direct contact area measurement.

### **4.3. Results**

#### **4.3.1 Kinematics**

The kinematics were obtained through image registration of the bones without cartilage. Kinematics for each specimen were unique (Table 4.3), because of the unique geometry of each specimen's bones and the fact that the initial position before loads were applied to the five tendons was different for each specimen.

Specimen 3 showed the highest magnitude of translation. The magnitude of lunate translation was 3.55 mm, and the magnitude of the scaphoid translation was 2.76 mm (Fig. 4.10). Specimen 3 also showed the highest magnitude of rotation. The magnitude of the lunate rotation was 0.24 degrees and the scaphoid rotation was 0.23 degrees (Fig. 4.11). Overall, the translation in the Z direction (dorsal-volar) showed the highest translation. This result is consistent with the dorsal contact shown in computational models. Because there was not a consistent translational trend; the bones did not always move in the positive or negative direction along a specific axis, the average translational magnitude could be misleading data and is not reported here.

The lunate and scaphoid rotations are very small. Over the five specimens, the average rotation was less than 0.2 degrees for both the lunate and scaphoid bones.

**Table 4.3** Kinematics for the scaphoid and lunate bones. Translation vector in millimeters, attitude vector units in degrees.

			X (M-L)	Y (D-P)	Z (A-P)
S1	Lunate	Translation	0.15	1.27	-1.77
		Attitude	0.09	0.12	0.05
	Scaphoid	Translation	-0.06	1.22	-1.15
		Attitude	0.02	0.10	0.04
S2	Lunate	Translation	-0.84	0.51	-1.51
		Attitude	0.00	-0.04	0.02
	Scaphoid	Translation	-0.21	0.89	-1.20
		Attitude	0.02	0.00	-0.02
S3	Lunate	Translation	-2.77	1.47	1.66
		Attitude	-0.18	-0.11	-0.11
	Scaphoid	Translation	-1.84	2.01	0.43
		Attitude	-0.18	-0.12	-0.09
S4	Lunate	Translation	0.84	-0.33	-1.43
		Attitude	-0.08	-0.16	0.04
	Scaphoid	Translation	-0.26	0.28	-1.61
		Attitude	0.03	0.13	0.07
S5	Lunate	Translation	0.83	1.09	-0.84
		Attitude	0.23	0.01	-0.06
	Scaphoid	Translation	0.92	0.21	-2.34
		Attitude	0.18	-0.02	-0.12

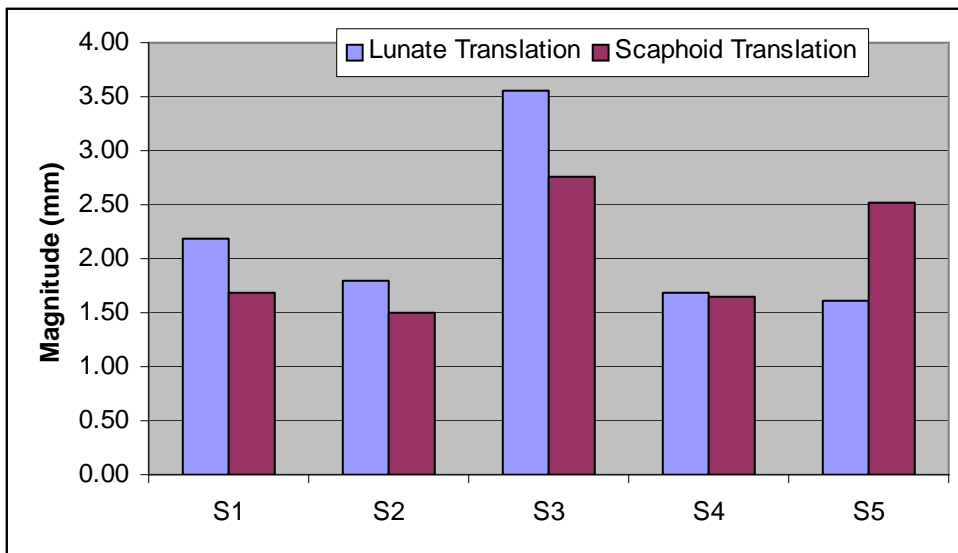


**Figure 4.10** Magnitude of translation of each specimen.

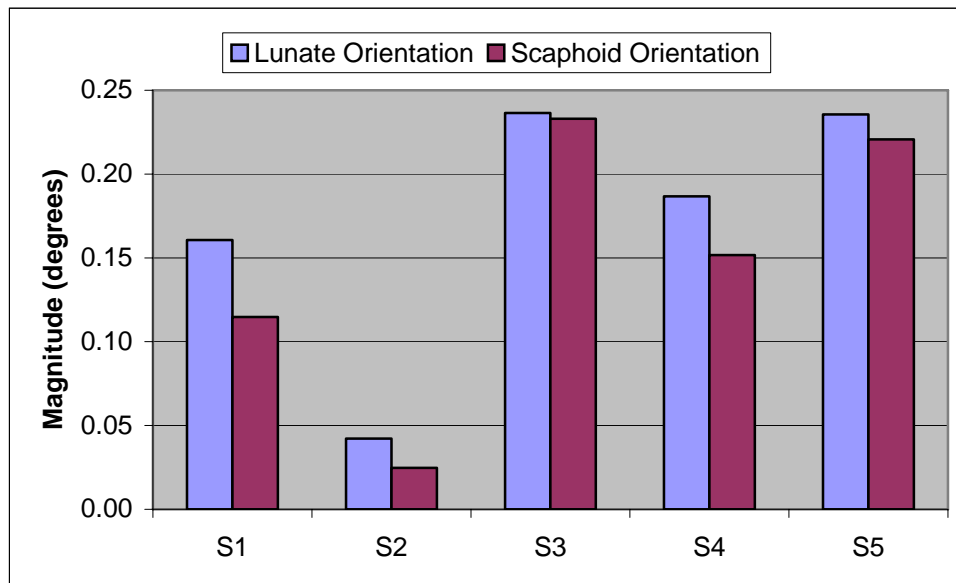


**Figure 4.11** Magnitude of rotation in degrees.

### **4.3.2 Summary of Experimental and Modeling Data**

The MRI-based models for all five specimens predicted contact areas, contact forces, and peak pressures with reasonable accuracy (Table 4.4). With the exception of Specimen 2, the sum of the contact forces was less than or approximately equal to the 110 N applied to the joint during testing (Fig. 4.12). Furthermore, it has been shown that percentage of total force carried in the scaphoid fossa of the wrist during grasp is about 50% of total applied force, and the total force carried through the lunar fossa during grasp is about 35% of total. The remainder is carried through the triangular fibro-cartilage complex.<sup>17</sup> Because only the radiocarpal contacts are measured in this experiment, these percentages change. The scaphoid fossa would carry 50% of 85% of total load, or 59% of measured load. The lunar fossa would carry 35% of 85% of total load, or 41% of measured load. These percentages generally agree with the data, especially the data from the MRI-based models. For all specimens, the MRI-based model predicted higher contact force (average 59% of measured load) and higher contact area in the radioscapoid fossa as compared to the radiolunate fossa (average 41% of measured load). The average predicted load ratio was 1.9 between the two joints, and the average predicted contact area ratio was 1.4 between the joints (Table 4.5).

**Table 4.4** Results of experimental data and MRI-based model. Radioscaphoid (R-S) and radiolunate (R-L) data shown here.

Spec	Peak Pressure (MPa)			Contact Force (N)			Contact Area (mm <sup>2</sup> )				
	Film	Tek	Model	Film	Tek	Model	Film	Tek	Model	Direct	
R-S	S1	2.47	1.82	2.42	86.70	43.10	71.97	32.00	91.00	57.08	50.12
	S2	2.66	1.70	2.39	146.90	62.00	138.00	55.40	94.35	129.70	65.99
	S3	2.10	1.38	2.16	67.19	54.27	57.20	31.98	29.03	47.65	45.21
	S4	1.85	1.50	1.98	87.17	59.65	66.20	47.17	65.32	71.43	65.65
	S5	1.18	2.75	2.26	32.81	53.73	63.52	32.81	70.11	70.05	77.5
R-L	S1	3.78	1.02	1.49	75.00	34.80	23.80	20.00	76.00	32.63	31.14
	S2	2.50	1.60	2.52	36.42	98.00	110.00	14.56	105.20	110.70	55.48
	S3	0.90	1.66	2.23	28.71	36.27	32.03	13.80	18.11	27.93	29.2
	S4	0.60	1.35	1.30	11.29	39.43	30.98	18.67	51.66	52.75	50.94
	S5	1.21	1.18	1.98	12.53	42.27	52.75	12.53	59.04	57.71	51.57

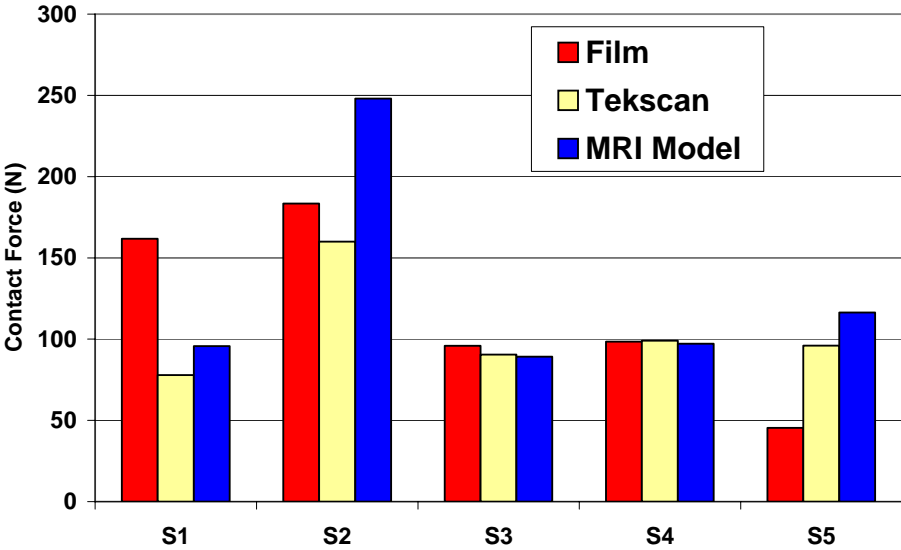


**Figure 4.12** Total Force measured by film, Tekscan sensor and MRI-based model.

Theoretically, value should be between 85-100 N.

Peak pressures from the MRI-based models were generally quite close to those from Pressurex film, and Tekscan peak pressures were generally lower than Pressurex or MRI-based models. Pressurex was less consistent for force (both over- and underestimating), and Tekscan was generally quite accurate compare to the total force applied. MRI-based models were similar to Tekscan providing consistently good measurement of total force (except for Specimen 2).

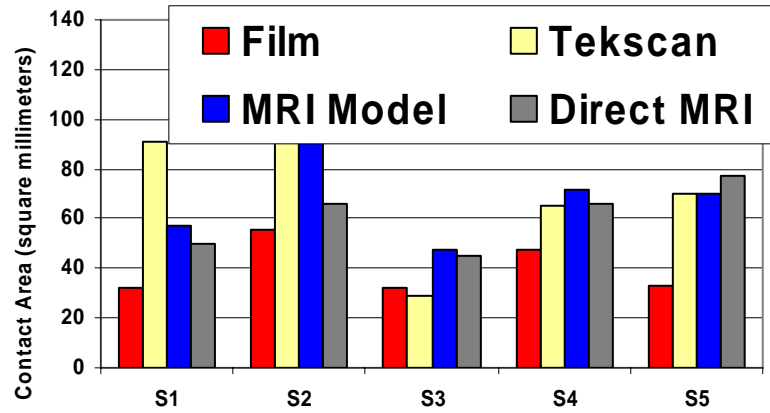
**Table 4.5** Comparison of contact load and contact area results from the MRI-based models between radioscapoid joint and radiolunate joint (expressed as a ratio).

Specimen	Ratio of RS to RL Force	Ratio of RS to RL Area
1	3.02	1.75
2	1.25	1.17
3	1.79	1.71
4	2.14	1.35
5	1.20	1.21
Average	1.88	1.44

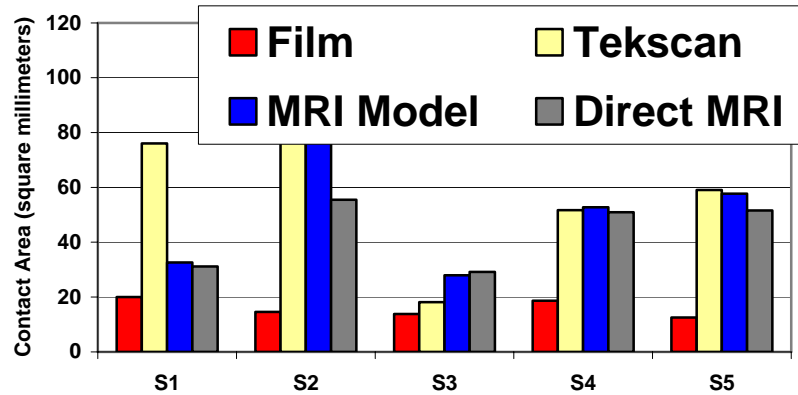
#### 4.3.3 Direct Contact Area Measurement

One method in this study was first implemented by Thoomukuntla, to compare the results from the MRI-based model with the direct measurement/calculation of joint contact from that apparent on the MR images.<sup>27</sup> Results between the contact model and the direct measurement show excellent agreement, with the exception of Specimen 2 (Table 4.4, Fig. 4.13 a,b). Once again, with the exception of specimen 2, all MRI-based contact areas of specimen-specific direct contact area measurements

for the radioscapoid and radiolunate fossa were within 12% of specimen-specific direct contact area measurements, with the average difference of 7%.



(a)



(b)

**Figure 4.13** Comparison of experimental measures, MRI-based method and direct contact area measurements for all five specimens. Radioscapoid joint (a) and radiolunate joint (b) shown here.

#### 4.3.4 Regression Analysis

Statistical analysis was performed to see what, if any, correlation existed between sets of data. Because specimen 2 had consistently questionable data, it was considered an outlier. Although not all data for specimen 2 confirmed it as a “statistical outlier” ( $\geq 3$  standard deviations from the mean), the lack of consistent data and the clear errors from all measures of force showed that the results for specimen 2 could not be trusted.

Although the Tekscan force data qualitatively appears to correlate well with the model data, it was not found to reach significance ( $p = 0.07$ ). The Pressurex data was clearly not significant, with  $p = 0.36$ . For pressure, once again the Tekscan sensor data and Pressurex film data were compared to the MRI-based model results. In this case, neither measurement technique was found to have significance, though the Pressurex film was closer, with  $p = 0.24$ , and the Tekscan having  $p = 0.54$ .

The last set analyzed was the contact area measurement. The direct measurement technique was found to have a strong linear correlation to the MRI-based model data, with  $p = 0.0002$ . When graphed, with the x-axis representing the direct contact area measurement values, and the y-axis representing the MRI-based model contact area results, a coefficient slope of 0.978 was found. Neither the Tekscan sensor data nor Pressurex film data were found to be significant, both having p values greater than 0.25.

Correlation coefficients were consistent with significance values. The only correlation value of interest was the direct contact area measurement compared to MRI-based model contact area measurement. In that case, the correlation coefficient was 0.91 (Fig. 4.14)

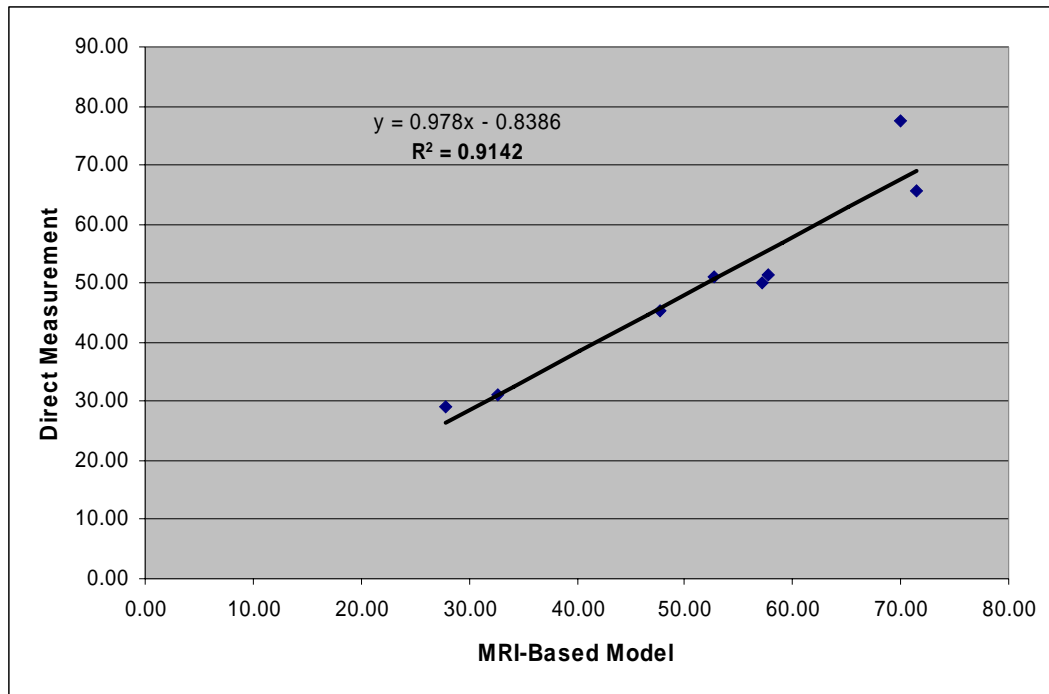


**Figure 4.14** Plot of contact area measurement from direct-measurement method versus contact area reported from MRI-based model.

#### 4.4. Discussion

The results of this work are promising. The specimens behaved consistently, and the MRI-based models yielded reasonable results.

Specimen 2 produced questionable data. One hypothesis is that the experimental technique was still being revised and developed when this specimen was tested. Although it is difficult to find a single reason why the Pressurex film, Tekscan sensor, and MRI-based model all resulted in joint contact forces well above the 110 N applied, there are independent reasons that may explain them all. The image quality of specimen two was poorer than any of the others. This may have resulted in lower quality models, as well as less accurate kinematic descriptions of the lunate and scaphoid movement during simulated grasp. Transverse shear was not likely to have been an issue. Kinematics do not indicate that the bones slid a large amount against one another when the load was applied. Lastly, the Tekscan sensors were sometimes trimmed along the edges, to allow them to better fit into the radiocarpal joint. The #4201 sensor is designed to cross the entire radiocarpal and ulnocarpal joint surface, but can be easily trimmed without damaging the sensor. Once the sensor had been trimmed, it had to be resealed tightly or else fluid would enter the sensor, and cause it to report false data. Fluid seepage is a possible cause of poor Tekscan data for specimen 2.

As far as the other specimens are concerned, the Pressurex film and Tekscan sensors both worked reasonably well. It was noted previously that data from Tekscan sensors and Pressurex film, although potentially accurate, are considered as relatively rough measures. Our tests show that 80% of measurements will have an accuracy of 11% or better for the Tekscan sensor, and that 80% of measurements will have an accuracy of 17.9 % or better for the Pressurex film.

The MRI-based model data was close to the Tekscan and Pressurex data. In general, the MRI-based model peak pressure data more closely resembles the Pressurex film results. This is likely because of the higher resolution of the Pressurex film over the Tekscan sensor. It is possible that the region of highest pressure was distributed over the low-resolution sensor of the Tekscan sensor, effectively hiding a peak pressure point. Further, the contact force reported from the model more closely matched the Tekscan sensor and not the Pressurex film. The most likely reason for this is the dynamic calculation of the Tekscan sensor as opposed to the Pressurex film. Because the film captures any pressure data, it can erroneously display “data” acquired during insertion and removal and during the process of loading/unloading the specimen. The dynamic data capture of the Tekscan sensor eliminates this artifact problem, and as the MRI-based model was created from images taken while the specimens were loaded and stable, it makes sense the Tekscan sensor data would more closely match the MRI-based model joint contact load data.

This theory is supported by the statistical analysis. Although it wasn't statistically significant ( $p < 0.05$ ), the Tekscan force data ( $p = 0.07$ ) did show a closer match to the MRI-based model data than the Pressurex film force data ( $p = 0.36$ ). Furthermore, the lack of any statistical significance of any experimental measure for pressure, contact area, or contact force provides evidence of the difficulty when using an experimental measure as a validation standard.

These five specimens build upon the three specimens previously tested by Thoomukuntla et al. using a similar technique.<sup>27</sup> Although Thoomukuntla did not load

the two wrist extensor tendons, simulated grasp was achieved using the finger flexors and taping the hand to the base plate, forcing it into neutral position. The results of these five specimens are consistent with the results of that work. The peak pressures found in these five specimen-specific MRI-based models are within a similar range (1.3 – 2.5 MPa) to the specimen-specific models tested in the previous study (1.0 – 2.1 MPa). Also, refinements in experimental technique allowed for a closer match between the direct MRI measured contact area and the contact area found in the MRI-based model.

The results of this study show that an MRI-based model used to calculate *in vivo* joint forces is feasible and possible. The specimens tested showed consistent results, and the experimental methods produced results sufficiently similar to the MRI-based model to consider the model effective in the prediction of joint peak pressure, contact force, and contact area. Because the method appears sound, but experimental data has too much error to be considered a gold standard, the next step in this process is to develop a method to validate the MRI-based model without inconsistent experimental measures like Tekscan and Pressurex. One measure in this process is the direct contact area measurement. This measure was used in this study, and showed very good correlation with the model data. Another method would be to compare cartilage deformation maps from cartilage directly segmented from unloaded and loaded MRI scans with MRI-based model deformation data.<sup>10, 11</sup> Further *in vivo* studies on living human subjects using these two techniques represent the next phase in the development of this modeling and measurement technique.

#### 4.5. References

1. Ahn HS, DiAngelo DJ. Biomechanical testing simulation of a cadaver spine specimen: development and evaluation study. *Spine* 2007;32(11):E330-6.
2. Anderson AE, Peters CL, Tuttle BD, Weiss JA. Subject-specific finite element model of the pelvis: development, validation and sensitivity studies. *J Biomech Eng* 2005;127(3):364-73.
3. Anderson DD, Daniel TE. A contact-coupled finite element analysis of the radiocarpal joint. *Semin Arthroplasty* 1995;6(1):30-6.
4. Anderson DD, Deshpande BR, Daniel TE, Baratz ME. A three-dimensional finite element model of the radiocarpal joint: distal radius fracture step-off and stress transfer. *Iowa Orthop J* 2005;25:108-17.
5. Anderson DD, Goldsworthy JK, Li W, James Rudert M, Tochigi Y, Brown TD. Physical validation of a patient-specific contact finite element model of the ankle. *J Biomech* 2007;40(8):1662-9.
6. Beek M, Koolstra JH, van Ruijven LJ, van Eijden TM. Three-dimensional finite element analysis of the cartilaginous structures in the human temporomandibular joint. *J Dent Res* 2001;80(10):1913-8.
7. Buchler P, Ramaniraka NA, Rakotomanana LR, Iannotti JP, Farron A. A finite element model of the shoulder: application to the comparison of normal and osteoarthritic joints. *Clin Biomech (Bristol, Avon)* 2002;17(9-10):630-9.

8. Carrigan SD, Whiteside RA, Pichora DR, Small CF. Development of a three-dimensional finite element model for carpal load transmission in a static neutral posture. *Ann Biomed Eng* 2003;31(6):718-25.
9. Donahue TL, Hull ML, Rashid MM, Jacobs CR. A finite element model of the human knee joint for the study of tibio-femoral contact. *J Biomech Eng* 2002;124(3):273-80.
10. Eckstein F, Glaser C. Measuring cartilage morphology with quantitative magnetic resonance imaging. *Semin Musculoskelet Radiol* 2004;8(4):329-53.
11. Eckstein F, Lemberger B, Gratzke C, Hudelmaier M, Glaser C, Englmeier KH, Reiser M. In vivo cartilage deformation after different types of activity and its dependence on physical training status. *Ann Rheum Dis* 2005;64(2):291-5.
12. Fregly BJ, Bei Y, Sylvester ME. Experimental evaluation of an elastic foundation model to predict contact pressures in knee replacements. *J Biomech* 2003;36(11):1659-68.
13. Fregly BJ, Sawyer WG, Harman MK, Banks SA. Computational wear prediction of a total knee replacement from in vivo kinematics. *J Biomech* 2005;38(2):305-14.
14. Gardiner JC, Weiss JA. Subject-specific finite element analysis of the human medial collateral ligament during valgus knee loading. *J Orthop Res* 2003;21(6):1098-106.
15. Genda E, Horii E. Theoretical stress analysis in wrist joint--neutral position and functional position. *J Hand Surg [Br]* 2000;25(3):292-5.

16. Genda E, Konishi N, Hasegawa Y, Miura T. A computer simulation study of normal and abnormal hip joint contact pressure. *Arch Orthop Trauma Surg* 1995;114(4):202-6.
17. Horii E, Garcia-Elias M, Bishop AT, Cooney WP, Linscheid RL, Chao EY. Effect on force transmission across the carpus in procedures used to treat Kienbock's disease. *J Hand Surg [Am]* 1990;15(3):393-400.
18. Koolstra JH, van Eijden TM. Combined finite-element and rigid-body analysis of human jaw joint dynamics. *J Biomech* 2005;38(12):2431-9.
19. Kwak SD, Blankevoort L, Ateshian GA. A Mathematical Formulation for 3D Quasi-Static Multibody Models of Diarthrodial Joints. *Comput Methods Biomech Biomed Engin* 2000;3(1):41-64.
20. Li G, Gil J, Kanamori A, Woo SL. A validated three-dimensional computational model of a human knee joint. *J Biomech Eng* 1999;121(6):657-62.
21. Li Z, Alonso JE, Kim JE, Davidson JS, Etheridge BS, Eberhardt AW. Three-dimensional finite element models of the human pubic symphysis with viscohyperelastic soft tissues. *Ann Biomed Eng* 2006;34(9):1452-62.
22. Manal K, Lu X, Nieuwenhuis MK, Helders PJ, Buchanan TS. Force transmission through the juvenile idiopathic arthritic wrist: a novel approach using a sliding rigid body spring model. *J Biomech* 2002;35(1):125-33.
23. Mesfar W, Shirazi-Adl A. Biomechanics of the knee joint in flexion under various quadriceps forces. *Knee* 2005;12(6):424-34.

24. Penrose JM, Holt GM, Beaugonin M, Hose DR. Development of an accurate three-dimensional finite element knee model. *Comput Methods Biomech Biomed Engin* 2002;5(4):291-300.
25. Pillai RR, Thoomukuntla B, Ateshian GA, Fischer KJ. MRI-based modeling for evaluation of in vivo contact mechanics in the human wrist during active light grasp. *J Biomech* 2007.
26. Taddei F, Pancanti A, Viceconti M. An improved method for the automatic mapping of computed tomography numbers onto finite element models. *Med Eng Phys* 2004;26(1):61-9.
27. Thoomukuntla, B.R., Master's Thesis: Preliminary Validation of MRI-Based Modeling for Joint Contact Mechanics. Mechanical Engineering, University of Kansas, 2005
28. Tsumura H, Miura H, Iwamoto Y. Three-dimensional pressure distribution of the human hip joint--comparison between normal hips and dysplastic hips. *Fukuoka Igaku Zasshi* 1998;89(4):109-18.
29. Ueki K, Nakagawa K, Takatsuka S, Yamamoto E. The change of stress distribution on the condyle after mandibular setback surgery. *Eur J Orthod* 2006;28(5):433-9.
30. Woltring HJ. 3-D attitude representation of human joints: a standardization proposal. *J Biomech* 1994;27(12):1399-414.

## Chapter 5. Summary

The results of this study show that MRI-based contact models of the wrist can indeed model the contact mechanics of the human wrist. The MRI-based models have accuracy at least as good as current experimental techniques, and likely even better.

### 5.1 Accuracy and Repeatability of Tekscan and Pressurex Sensors

Six sets of tests were run. Each test began by first performing an individual calibration and then testing each sensor with contact of two cylindrical objects covered in 80A rubber. The Pressurex film and Tekscan sensor were pressed with loads ranging from 100 to 700 N in 100 N increments with these two cylinders. Using the test-specific ten point calibration curve, the pressure sensor was used to measure the load applied by the cylindrical object. These values were compared to the actual applied load values. Each time a test was run, a new calibration strip was made for the Pressurex, to eliminate variability caused by changing temperature and humidity. A new calibration was also performed for each Tekscan sensor test.

It was shown that the accuracy and repeatability of the Tekscan sensor as well as Pressurex film are only high enough to use them as a “ballpark” value near which the MRI-based model will predict. Under ideal conditions, the Tekscan sensor had an 80% confidence interval of 11.1% error, and a 95% confidence interval of 17.0% error. Given the complex geometry of the radiocarpal joint, and the variable loading conditions during simulated grasp, it was shown that the ideal condition is never

present, and so accuracy and repeatability will be worse. It was also shown that the Pressurex film was less capable of predicting loads, as the 80% confidence interval was 17.9% error, and the 95% confidence interval was 21.5%. Furthermore, the sensitivity to damage from fluids made Pressurex film difficult to use in wet human joint studies.

These results have far-reaching implications for joint model validation studies. If experimental data cannot be counted on to be accurate in *in vitro* work, then can a model whose results are compared to the experimental data be considered accurate and validated? Furthermore, the Tekscan sensor and Pressurex film became less accurate under low loads. Often at low loads, the Pressurex film would only show scattered redness that was difficult to measure and it was especially difficult to define the bounds of the contact region. The Tekscan sensor would either ignore low loads completely or randomly show and hide them, making snapshots of the sensor data difficult to believe. At high loads, both sensor types suffered from saturation, as the Pressurex film would completely saturate red, and the Tekscan sensor would reach its maximum digital output value and go no higher. Often, it would be possible to adjust the gain on the Tekscan sensor, and move it into a more ideal range for the testing. However, the sensor is still limited in that it would drop out low activated sensels if the gain was too low, and it would saturate highly activated sensels if the gain was too high.

Both the Pressurex film and Tekscan sensor did show a reasonable level of accuracy in this validation study. Although in specimen two, all three measures

(Tekscan, Pressurex, MRI-based) reported loads far higher than the loads actually applied, for the most part both the Tekscan sensor and Pressurex film yielded results that can be considered helpful. The data they produce, however, cannot be considered exact for joint mechanics or other problems.

## **5.2 Segmented Cartilage Models vs. Cartilage Models Projected from Bones**

Three human cadaver wrists were imaged using a 9.4T MRI scanner. The wrists were imaged in both relaxed position as well as in simulated grasp. 3D models were then generated of the radius, scaphoid, and lunate bones. Two sets of models were created, one using the bone and cartilage, and another using only the bone. To the latter model a cartilage layer was “projected” 1 mm normal to the surface of the bone. The two models were then used, along with the same kinematic description, to calculate the forces in the radiocarpal joint. Model results were compared to experimental data gathered using Tekscan sensors.

It was shown that segmented models of bones and cartilage in small, geometrically complex joints are superior in their modeling accuracy than projected cartilage models. The models created with projected cartilage often predicted joint contact loads far higher than the segmented cartilage models predicted. Also, the cartilage models were closer to the experimental data than the projected cartilage models.

Volumetric data was also significant. The volumes of the projected cartilage models did not consistently overestimate or underestimate compared to the directly

segmented models; in some cases it overestimated, and in others underestimated. If one assumes the directly segmented cartilage models are geometrically accurate, then it can be said that the projected cartilage models do not represent an accurate imitation of the bones and cartilage in the joint.

This has implications in several branches of computational biomechanics. Rigid body spring models (RBSM) as well as finite element models are often built using bone data with projected cartilage layers. Although those studies have shown reasonable results, the results shown here indicate that care must be taken to ensure the projected cartilage layer is consistent with the actual cartilage.

### **5.3 Validation of an MRI-based Joint Model**

Five human cadaver wrists were studied. The forearms were dissected, and five tendons were isolated. These tendons were given individual loads totaling 110 N to simulate grasp of the hand. The hands were then imaged in a 9.4T MRI scanner. The specimens were also loaded after either a Tekscan sensor or Pressurex film had been inserted in the radiocarpal joint, as done in section 4. Experimental models were created of the radius, lunate, and scaphoid bones, and kinematics were found of the bone motion from the unloaded to loaded case. The bone models were then input into the Joint\_Model program, along with the kinematics, and models predicted the contact area, contact force, and peak pressure in the radioscapoid, radiolunate, and scapholunate joints. These data were compared to the Tekscan and Pressurex results, as well as to a direct contact area measurement taken from the MR image sets.

It was found that the MRI-based models were consistent with the experimental data. The MRI-based models predicted peak pressures which closely matched the Pressurex film. The Tekscan sensor showed a contact force similar to the MRI-based model. Finally, the direct contact area measurements were very similar to the MRI-based contact area, for both joints.

This shows that the MRI-based modeling technique is feasible. However, the method has been shown to be sensitive to image quality; specimen 2 had the worst quality images, and the poorest correspondence to experimental data. Specimen 2 also overestimated the contact force significantly, which may be attributed to either poor kinematic description, poor models, or both. Further, the quality of images has a two-fold impact. Kinematic registration is based on normalized mutual information, and the better the image quality, the more likely accurate kinematics will be obtained. The second impact is that the segmentation of cartilage surfaces is highly dependent on image quality. Improvement of the image will lead to more accurate models, and data can be more confidently analyzed.

#### **5.4 Implications for Future Work**

The next phase of this work will be to begin human subject work. Because the experimental data was shown to be only marginally accurate and helpful in validation only to a degree, then ideally a different method should be developed to validate the MRI-based model. One method is the direct measurement of contact area from the MRI images. This method showed good correlation with the contact areas predicted

in the MRI-based model, and should be pursued as a method of validation. Another benefit of this method is that it does not require invasive procedures, and therefore will work well with live subject studies.

Another technique to investigate would be direct measurement of cartilage deformation from the MR images. If the deformation of the cartilage layers was measurable, then it would be possible to compare with model data. These models have the advantage of calculating the stresses on that cartilage.

These two methods should provide a good approach to further validate the MRI-based modeling technique, as well as allow a transition to human subject testing.